




Exogenic dust inventory in the Saturn system: the *Cassini* Cosmic Dust Analyzer perspective

Nicolas Altobelli¹  ¹★, Frank Postberg,² Sascha Kempf,³ Andrew R. Poppe⁴ , Jürgen Schmidt,² Christian Fischer,⁵ Georg Moragas-Klostermeyer⁶ and Ralf Srama⁶ 

¹European Space Astronomy Center (ESA/ESAC), Madrid, 28692, Spain

²Freie Universität Berlin, Berlin, 14195, Germany

³University of Colorado, LASP, Boulder, CO-80303-7814, USA

⁴Space Sciences Laboratory, University of California, Berkeley, 94720, USA

⁵Institute for Geophysics, Heidelberg, 69120, Germany

⁶University of Stuttgart, Stuttgart, 700049, Germany

Accepted 2025 April 7. Received 2025 April 5; in original form 2024 June 29

ABSTRACT

We constrain the inventory of exogenic dust populations found in the Saturn system by analysing 14 yr of *Cassini* Cosmic Dust Analyzer (CDA) data acquired since Saturn orbit insertion. Our analysis reveals that the Saturn system is permanently traversed by exogenic dust coming from the surrounding interplanetary space, interplanetary dust particles (IDPs), and from the interstellar medium, interstellar dust (ISD). The CDA data give a first *in situ* experimental insight into the different dust populations of the outer Solar system and their relative abundances. We observe a population of sub-micron to tens of micron-sized interplanetary grains, with low injection speed at Saturn's Hill's boundary, and whose dynamical signature supports their collisional origin in the Edgeworth Kuiper belt or a release upon cometary activity of Jupiter-family comets and Centaurs. We confirm that those populations are the most abundant IDP population in the Saturn system, participating to the weathering of the surfaces of the icy moons and the rings. We also observe the signature of sub-micron grains with high injection speeds at Saturn's Hill's radius, bearing the dynamical signature of dust released by Oort cloud comets. In addition, a population of large ISD grains appears clearly in our data, in the micrometre-sized regime, hence larger than detected *in situ* by previous missions and analysis. Finally, we also find hints of an extended dust halo of bound particles, reaching high latitudes in the inner Saturn system as well as possible sporadic sources of interplanetary grains.

Key words: methods: data analysis – space vehicles: instruments – comets: general – interplanetary medium.

1 INTRODUCTION

We use in this paper data of the *Cassini* Cosmic Dust Analyzer (CDA) obtained in the Saturnian system between 2004 and 2017 in order to identify dust particles originating from outside the Saturnian system, called hereafter exogenic dust. Finding such exogenic particles and constraining their origin is of importance to support a variety of investigations performed by *Cassini* in the Saturn system. For instance, the formation and compositional evolution scenarios of the main rings rely on a detailed understanding of their erosion by exogenic projectiles, resulting in regolith growth on individual ring particles and compositional mixing through ballistic transport of ejecta (Cook & Franklin 1970; Durisen 1984; Cuzzi & Durisen 1990; Cuzzi & Estrada 1998; Tiscareno et al. 2013). Modelling by Elliott & Esposito (2011) confirmed that ring regions containing less mass (optically thinner) would be more compositionally mixed (as by a greater alteration of their reflectance spectra) with the in-falling dark exogenic material. Through a derivation of the total

exogenic dust mass influx on to the rings, Kempf et al. (2023) could constrain the age of Saturn's rings. Also, quantifying the amount of exogenic elements being delivered to the inner Saturn system is important for detailed studies of the stratospheric photochemistry of Saturn and Titan (Coustenis et al. 1998; Moses et al. 2000; Fouchet, Bézard & Encrenaz 2005; Moses & Poppe 2017). Finally, grains of interplanetary origin impacting the atmosphere-less surface of Saturn's icy moons yield ejecta that form dusty exospheres (Spahn et al. 2006a; Jones et al. 2008) and tenuous rings (Hedman et al. 2009; Verbiscer, Skrutskie & Hamilton 2009), or that transport and redistribute non-icy contaminant material across the Saturnian system (Filacchione et al. 2013). It is also important to subtract this population from Saturn-bound particles, especially in the outer Saturn system, in order to identify the material released from Saturn's moons.

Beyond the relevance for the investigation of the Saturnian system, studying exogenic dust at Saturn is an opportunity to learn more about the populations of interplanetary material in the outer Solar system. The spiral structures detected in the C and D rings of Saturn (Hedman et al. 2011; Hedman, Burns & Showalter 2015) and in the Jupiter ring system (Showalter, Hedman & Burns 2011) give direct evidence that

* E-mail: nicolas.altobelli@esa.int

streams of interplanetary particles traverse sporadically the regions close to the giant planets. Signatures of impacts of such particles on Saturn's rings were directly detected in *Cassini* images (Tiscareno et al. 2013).

While dust populations are relatively well characterized in the inner Solar system from both remote sensing and *in situ* observations, measurements of dust populations beyond the orbit of Jupiter are rather sparse. Before *Cassini*, three spacecraft equipped with dust instruments have measured the flux of dust particles at Saturn heliocentric distance: *Pioneer 10* and *Pioneer 11* as reported in Humes (1980) and Landgraf et al. (2002) and more recently the Student Dust Counter (SDC) onboard *New Horizons*, now transiting through the Edgeworth Kuiper belt (Poppe et al. 2010; Szalay, Piquette & Horányi 2013; Piquette et al. 2019; Bernardoni et al. 2022; Doner et al. 2024). Those data were used to calibrate dynamical models for the interplanetary dust fluxes in the outer Solar system (Poppe 2016; Poppe et al. 2019). Also, the radio and plasma wave experiment onboard *Voyager 1* and *Voyager 2* detected dust in the outer Solar system (Gurnett et al. 1997). However, all these spacecraft spent a relatively short time at Saturn heliocentric distance. *Cassini* CDA, in turn, with a larger sensitive area and higher sensitivity than SDC, has been in orbit around Saturn from 2004 to 2017, and the continuously collected CDA data can be used for a long-term monitoring of the dust populations present around 10 au heliocentric distance, informing micro-meteoroid models of the outer Solar system.

The main focus of this work is to characterize the exogenic dust populations found within the Saturnian system using the *Cassini* CDA data, to constrain their possible origin, and to quantify their relative abundance. For composition analysis of Saturn's rings and exogenic grains using CDA data, we refer the reader to recent works such as Linti et al. (2024a, b) as well as Altobelli et al. (2016).

2 TRAJECTORY AND FRAME DESCRIPTIONS

Fig. 1, top panel, shows *Cassini*'s trajectory over the mission lifespan, covering about half an orbit of Saturn around the Sun. We use this plot to illustrate the definition of the Saturn Apex frame (named hereafter SAT_APEX). The X-axis is aligned with the velocity vector of Saturn with respect to the Sun and the Y-axis is the orthogonal component of the Sun-Saturn vector on the X-axis. To complete this frame to a right-handed frame, the Z-axis is perpendicular to Saturn's orbital plane, towards the ecliptic South. In this frame, for an observer 'sitting' on Saturn and looking towards Saturn's direction of motion, the Sun is 'on the left' (Fig. 1, bottom panel). The yellow dots show the small changes in solar direction over the *Cassini* mission lifespan due to the eccentricity of Saturn's orbit. This plot shows in addition the normalized relative cumulated coverage of the sky by the CDA field of view, combined for the chemical analyser target (CAT) and the impact ionization detector (IID) subsystems (see Fig. 3). Because the pointing history of CDA was determined by the scientific requirements of different instruments, measurement campaigns, and/or constrained by operational requirements, the coverage of Saturn's sky by CDA was not isotropic. The radiant direction of the interstellar dust (ISD) stream (Mann & Kimura 2000; Czechowski & Mann 2003; Landgraf et al. 2003; Sterken et al. 2012) is nearly wandering from the helion to the antihelion directions between 2004 and 2017, crossing Saturn's apex direction in 2009. The relatively high observation time accumulated by CDA towards the ISD direction is the result of dedicated observation campaigns in particular during the two extensions of the mission (2008–2017).

The relative, cumulative time spent by *Cassini* at different locations in the Saturn system is shown in Fig. 2. This plot shows that

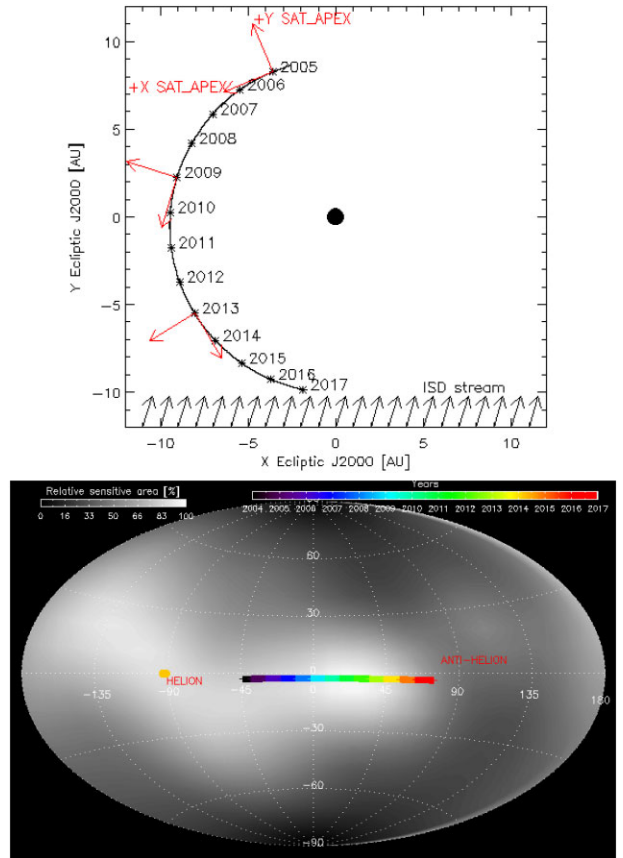


Figure 1. **Top panel:** Heliocentric trajectory of *Cassini* from the beginning to the end of the science mission at Saturn. The SAT_APEX frame, used in this paper, is illustrated by the red arrows (see text for definition). The direction of the ISD flux is indicated by the black arrows. **Bottom panel:** Normalized cumulative coverage of the sky by CDA in the SAT_APEX frame, using the combined field of view of the IID and CAT subsystems. The Sun radiant directions over the entire mission ('helion') are shown as orange dots – the radiant direction of the ISD stream is shown as a thick coloured line, coded by elapsed mission time.

Cassini's trajectory around Saturn spent significant time exploring regions north and south of the ring plane, which, as we will see, helped detecting exogenic grains.

3 DATA ANALYSIS

In the following sections, we present the data acquired by the entrance charge grid, also called entrance grid (EG), the CAT, and the IID of CDA (see Srama et al. 2004, their table 8). The technical drawing of CDA, as published in Srama et al. (2004), is shown in Fig. 3 to ease the reader's visualization of the different subsystems used in this paper. Each subsystem has its strengths and weaknesses to support our search for exogenic dust in the Saturn's system, including different sensitivity thresholds, making them sensitive to different particles sizes, requiring adapted analysis techniques. We then model our data in Section 4 and discuss the possible different origins and relative abundance of the exogenic particles.

The major difficulty we are facing to find exogenic dust particles in the Saturnian system is their low abundance in an environment dominated by E ring particles produced by the cryo-volcanic activity of Enceladus (Porco et al. 2006; Spahn et al. 2006a), making our study similar to 'looking for a needle in a haystack'. In the denser

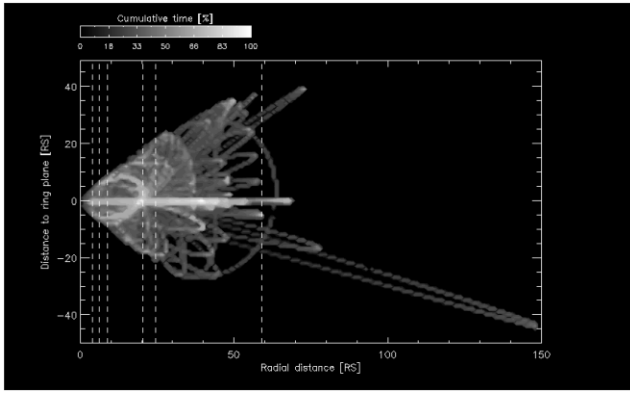


Figure 2. Cumulative time spent by *Cassini* in bins of radial distance and distance to the ring plane, from SOI until end of mission.

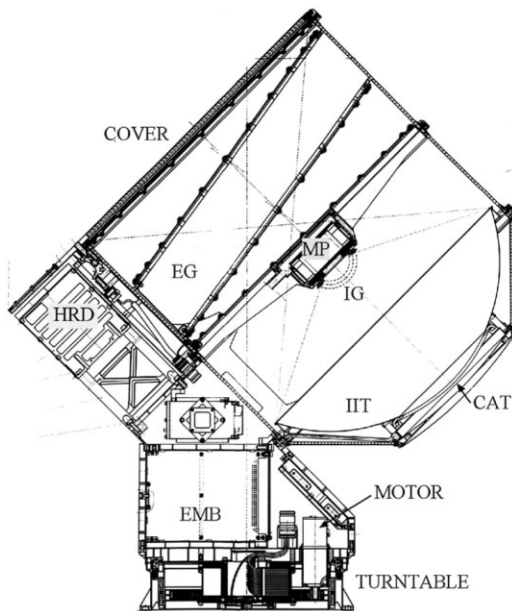


Figure 3. Technical drawing of the CDA: CAT (chemical analyser target); EG (entrance grids); EMB (electronics main box); HRD (high rate detector); IIG (ion grids); IIT (impact ionization target); and MP (multiplier). Note that IIT is also named IID (for impact ionization detector).

regions of the E ring, the CDA instrument is saturated by E ring dust detections, therefore ‘masking’ contributions from other sources. Fortunately, the *Cassini* spacecraft has been flying on orbits covering a wide range of inclinations (with respect to the ring plane, Fig. 2) and eccentricities while touring Saturn, traversing regions where the E ring is very dilute, a feature of the *Cassini* mission that we will exploit in our analysis. The CDA instrument was in measurement mode most of the time (with all its subsystems continuously on over 90 percent of the overall mission). Having measured nearly continuously for 13 yr provides enough integration time in these regions for our study to be done with sufficient statistics despite comparatively much lower abundance of exogenic dust at Saturn compared to ‘local’ populations.

3.1 Entrance grid subsystem data

We summarize here the key points of the EG data analysis method, first presented in Kempf et al. (2023), to derive the exogenic micro-

meteoroid mass flux on to the rings of Saturn. We then use the EG data to constrain the particles’ origin.

The CDA/EG subsystem is sensitive to the electrostatic charge carried by dust grains entering the instrument. The signal induced on the inclined conductive grids (referred to hereafter as ‘QP’, following the naming convention of the CDA channels described in Srama et al. 2004) can be used to constrain the dust grain’s velocity vector (Auer 1975; Kempf et al. 2004; Srama et al. 2004) and its charge. The grain charge is the result of the balance of different charging processes in space, as described in Horanyi, Burns & Hamilton (1992). For a simplified model of a spherical grain, the charge depends on the grain’s radius and equilibrium potential. The latter can be calculated for a known plasma environment at the location of detection, allowing to derive the equivalent grain radius from the QP detection. Contrary to the other CDA subsystems, IID and CAT, the grain mass cannot be derived directly, and requires an assumption on the grain’s density.

For the detections with EG, the lower grain size threshold is about 1–1.5 micron equivalent radius because smaller grains typically have a too low charge to produce a QP signal with sufficient signal-to-noise ratio. Therefore, the total number of QP events recorded (163) is relatively low compared to the data sets of the other subsystems because such large grains are relatively rare. Moreover, a QP detection requires favourable ambient plasma conditions to avoid grid saturation and/or poor signal-to-noise ratio. We analysed all QP events recorded since Saturn orbit insertion (SOI) that were detected outside the bulk of the E ring, because in that region CDA was typically saturated by the large E ring dust impact rate. While the speed can be measured with high accuracy with the EG subsystem, an indetermination remains on the third coordinate of the impact direction vector because the detector has only two grids. As a result, the number of impact velocity vectors that can explain the measured signal can range from 1 to 4 (see Kempf et al. 2023 for a detailed description of the determination of the velocity vectors).

For each event and impact velocity vector solution, the possible trajectory of the dust grain is propagated ‘backwards’, taking into account the gravity of Saturn and the Sun. The numerical method used for trajectory propagation is a Runge–Kutta–Nystroem algorithm with the symplectic Euler coefficients. In the grain size range relevant for the EG detector ($>1 \mu\text{m}$), the q/m ratio is small such that we can safely neglect the influence of Lorentz forces within Saturn’s magnetosphere. Furthermore, as the trajectory is computed for a short time-scale [of the order of the orbital period in the case of Saturn-bound solutions or the few months needed to reach the Hill sphere radius (RH) for exogenic grains], we can also neglect perturbations acting on a longer time-scale such as higher order gravity due to Saturn’s oblateness as well as the plasma drag and solar radiation forces. Trajectories that would lead to a collision with Saturn or the main ring are obviously not considered. For each grain, three cases can occur:

- (i) Each possible trajectory corresponds to an exogenic grain.
- (ii) Some trajectories imply a Saturn-bound orbit and some imply an exogenic origin.
- (iii) All possible solutions imply a Saturn-bound orbit.

Kempf et al. (2023) reported that at least 73 grains correspond to the first case above, and are therefore with certainty of exogenic origin (that is, an origin outside of the Saturn system), and additional 90 grains have at least 1 trajectory solution that implies an exogenic origin. The distribution of the particle speeds with respect to Saturn as they enter the system (also referred to as ‘injection speed’, practically, as they reach a distance to Saturn equal to the planet’s Hill’s radius $RH = 1100 \text{ RS}$) is plotted in Fig. 4. We include the injection speed

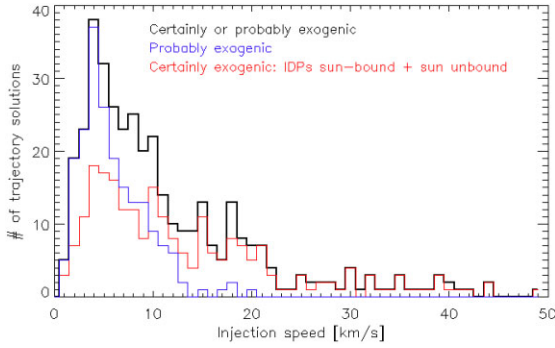


Figure 4. Distribution of the injection speed at 1 RH distance from Saturn, for all potentially exogenic solutions (in black). The particles having at least one exogenic solution (in blue) are considered as probably exogenic, and particles with all solutions exogenic (in red) are with certainty exogenic.

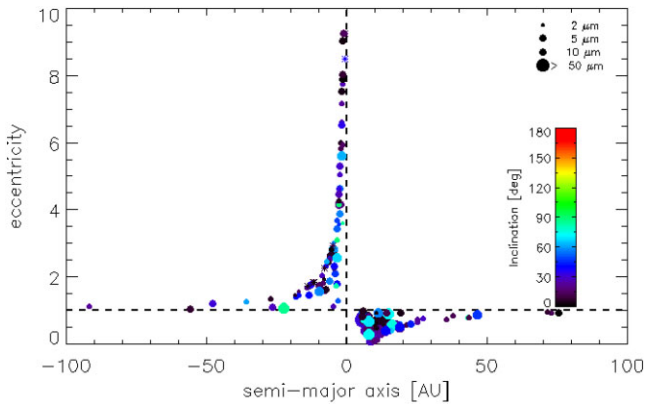


Figure 5. Heliocentric semimajor axis and eccentricity for confirmed exogenic particles in the EG data, on prograde solar orbits (bound and unbound). The colour coding indicates the heliocentric inclination (relative to the ecliptic J2000 frame), and the symbol size is proportional to the particle's radius. When the radius could not be derived, a star symbol is used.

distribution for all particles with at least one exogenic solution (probably exogenic grains) as well as for particles with all solutions exogenic (certainly exogenic grains). In both cases, the peak of the distribution of the injection speeds is around 4.5 km s^{-1} , with lower and upper limit values around 1 and 50 km s^{-1} , respectively.

For those grains being with certainty of exogenic origin, we determined the heliocentric velocity and position vectors when the particles crossed 1 RH distance from Saturn on their way into the system and we derived the corresponding heliocentric orbital elements in the ecliptic J2000 frame (Figs 5 and 6). Fig. 7 shows the injection points at 1 RH (radiant directions) inferred from all exogenic solutions of the EG data set, with a colour coding related to the heliocentric inclinations. We stress again at this point that, owing to the indetermination of one velocity vector component, one single particle detection can yield up to four possible impact velocity vectors, resulting in up to four different data points for the orbital elements. Keeping this uncertainty in mind, we analyse in the following paragraphs the distribution of the heliocentric semimajor axis a , eccentricities e , and inclinations i of the exogenic solutions, as well as their radiant direction at Saturn to constrain the particles' origins.

Considering Fig. 5 and Figs 6 and 7, we observe that EG exogenic grains can be divided in two main categories: particles on

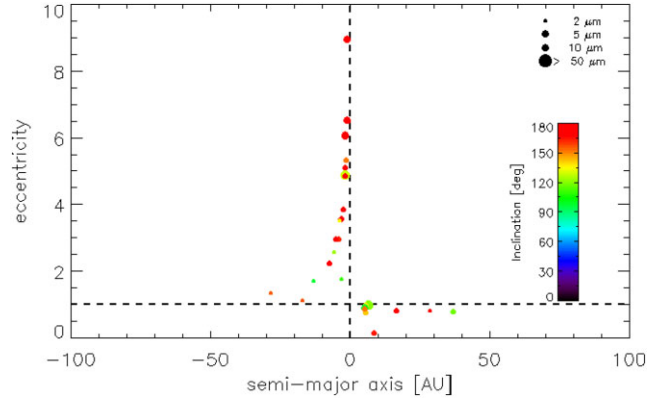


Figure 6. Heliocentric semimajor axis and eccentricity for confirmed exogenic particles in the EG data, on retrograde solar orbits (bound and unbound). The colour coding indicates the heliocentric inclination, and the symbol size is proportional to the particle's radius. When the radius could not be derived, a star symbol is used.

heliocentric bound orbits, referred to hereafter as interplanetary dust particles (IDPs), and particles on heliocentric unbound (hyperbolic) trajectories with high inclinations, including retrograde trajectories (inclination $> 90^\circ$).

We note that some grains stand out (Fig. 7), namely those with about 180° heliocentric inclination (in red) and whose radiant direction and heliocentric inclination coincide with the values expected for ISD grains during most of the *Cassini* mission (thin coloured line, see figure caption). While the presence and composition of sub-micron-sized ISD grains had been reported at Saturn using the CDA-CAT subsystem (Altobelli et al. 2016), large (in the micrometre-sized regime) ISD grains such as those revealed by the CDA-EG subsystem are here observed *in situ* for the first time. Such large ISD grains could not be detected via the CAT compositional analysis as performed by Altobelli et al. (2016) because the CAT subsystem does not provide resolved time-of-flight (TOF) spectra in the relevant grain sizes and impact velocity range.

As reported in Kempf et al. (2023), the peak of the injection velocity distribution for the prograde Sun-bound IDP particles ($e < 1$, $a > 0$, see Fig. 5) lies at relatively low speeds between 4 and 5 km s^{-1} . As shown in Fig. 7 (middle panel), they also have low-to-medium heliocentric inclinations. We refer hereafter to those particles as 'slow IDPs'. They represent the majority of the exogenic particles at Saturn.

In addition, we find a minority of IDPs having high inclinations, allowing in some cases for retrograde solar orbit (heliocentric inclinations larger than 90°). Those IDPs have high injection speeds (ranging from 10 to 40 km s^{-1}) and are referred hereafter as 'fast IDPs'.

Particles on solar hyperbolic orbits are found to be either prograde or retrograde (Figs 5 and 6), with a large span of eccentricities $e > 1$, from clearly hyperbolic ($e > 1$, $a < 0$) or near-parabolic orbits (eccentricities close to 1). Among the hyperbolic population, the ISD particles from the known ISD stream stand out, with heliocentric inclinations close to 180° , and crossing Saturn's apex direction, in agreement with the theoretical expectations (simulated radiant and inclination shown by the fine red line in Fig. 7). Those ISD grains are a subset of the dust population with high injection speeds at Saturn. Interestingly, a large fraction of the particles with hyperbolic trajectories do not belong to the well-known ISD stream (see Section 5).

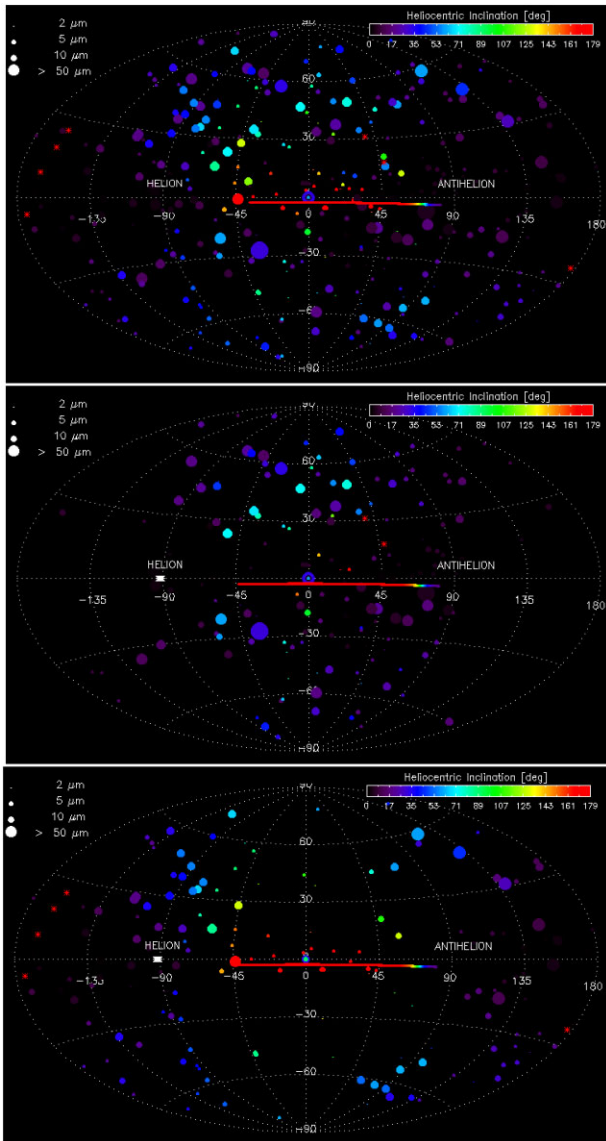


Figure 7. Radiant directions in the SAT_APEX frame, at 1 RH distance from Saturn, colour coded for heliocentric inclination of **top panel** (all exogenic particles detected by the EG subsystem); **middle panel** (Sun-bound particles); and **bottom panel** (Sun-unbound particles). The size of the circles is proportional to the particles' radius. The ISD stream's radiant direction is indicated by the thin line, colour coded for heliocentric inclination in the ecliptic J2000 frame. The Sun direction ('helion') is indicated by the white crosses.

3.2 Chemical analyser target data

The CAT subsystem of CDA provides a TOF mass spectrum, not only indicative of the elemental composition of the particles (Srama et al. 2004), but also of their minimum impact speed. To generate a proper TOF signal, a dust impact must occur on the specific CAT target located in the centre of, and surrounded by, the ring-shaped IID target. The sensitivity of the CAT subsystem allows to detect grains impacting with speeds larger than 3 km s^{-1} . However, the sensitivity of CAT is limited for large grains when too many ions are generated upon impact, the upper limit being 2 pC charge on the ion grid (QI) channel. Assuming a particle density of 2500 kg m^{-3} , this upper charge limit translates to a maximum detectable grain size of 0.5 micron radius for an impact speed of 20 km s^{-1} and up to 1 micron at

10 km s^{-1} . A specific TOF analysis technique is described in Fiege et al. (2014) and Altobelli et al. (2016) that provides the lower limit for the minimum impact velocity of particles based on an analysis of the oxygen line amplitude, within an uncertainty of less than 5 km s^{-1} . This technique is better adapted to our study of exogenic particles at Saturn, compared to the analysis of the rise time of the QI and chemical analyzer target (QC) signals, that yields at best a factor of 2 uncertainty in the velocity determination while a factor of (at maximum) $\sqrt{2}$ is needed to determine whether an orbit is bound or unbound.

An important assumption behind the analysis of the CAT data is that exogenic particles will contain rock-forming elements, and therefore form TOF spectra referred to hereafter as 'mineral', rather than forming pure 'water' spectra such as those known for the E ring particles. This assumption is reasonable if one keeps in mind the various sources of IDPs in the outer Solar system. Comets are an intricate mixture of volatile elements (including water) and silicates. For example, Jupiter-family comets (JFCs) and their dynamical precursors, Kuiper belt object (KBO) or Centaur objects, contain a large mineral mass fraction with a typical refractory-to-ice mass ratio of 3 (Fulle et al. 2019). In addition, even if ice-dominated grains of the size detected by *Cassini* were produced within the Kuiper belt, or by the cometary activity of nearby objects such as Trans-Neptunian Objects (TNOs) and Centaurs, only the rocky fraction is likely to reach Saturn: on the one hand, the ice sublimation temperature is reached at 10 au for $20 \text{ }\mu\text{m}$ particles (Mukai & Yamamoto 1979; Moro-Martín & Malhotra 2002), and, on the other hand, ultraviolet photosputtering models predict an efficient destruction of the icy component of dust grains well beyond the sublimation line (Grigorieva et al. 2007). Hence, while we do not exclude that a certain amount of water could be present in the exogenic particles entering Saturn's system, we consider safe to assume that exogenic dust of interplanetary (or interstellar) origin, detected at Saturn, cannot consist of pure water ice and it thus can be used as a unique discriminator from E ring grains.

All mineral grains in the CAT data set between 2004 and 2017 (1778 particles) have been identified and their minimum impact velocity derived, considering the spacecraft velocity with respect to Saturn, the CDA pointing at the time of impact, and the uncertainty on the determination of the impact direction resulting from the target half opening angle of 28° .

Fig. 8 shows the minimum speed relative to Saturn derived for all mineral grains (top panel). All those particles, whose speeds relative to Saturn are larger than the escape velocity at the distance of detection, are of exogenic origin. This plot also shows that many mineral grains exist in the Saturn system on bound orbits around the planet, in particular within Titan's orbital distance. We plot in the bottom panel of Fig. 8 only those CAT grains with exogenic origin (selecting them conservatively, ensuring that the lower limit value of their velocity is larger than the escape velocity). This plot shows that all mineral grains detected beyond Titan's orbit must have an exogenic origin. Furthermore, the speed values inferred for different radial distances are in agreement with injection speeds into the Saturn system ranging from 10 km s^{-1} to above 20 km s^{-1} if one takes into account the acceleration due to Saturn's gravitational focusing (computed using the analytical expression from Spahn et al. 2006a). Considering in addition the upper sensitivity of the CAT subsystem of 2 pC total charge allowing the generation of a proper TOF signal, the detected grains must have a maximum size of about $1 \text{ }\mu\text{m}$ equivalent radius for the standard silicate particle density of 2500 kg m^{-3} (Love, Joswiak & Brownlee 1994).

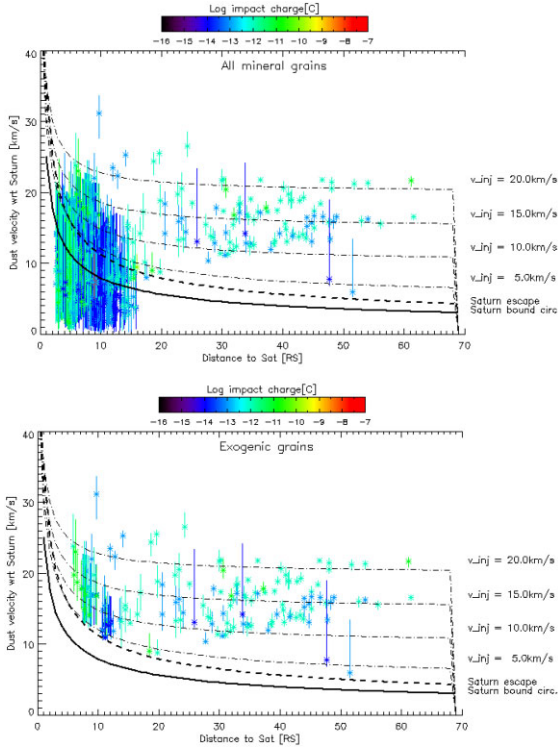


Figure 8. **Top panel:** Minimum velocities with respect to Saturn, inferred from the TOF spectra, of all mineral grains in the CAT data set, plotted as function of the radial distance to Saturn. The colour coding stands for the total ion impact charge generated upon impact. The vertical bars indicate the possible range of the minimum speed value, considering all possible impact directions within the CAT field of view. The black plain line indicates the speed of Keplerian circular orbits around Saturn, the dashed line indicates the escape speed, and the dot-dashed lines indicate the particles' speed relative to Saturn for different assumptions on the injection speeds at the Hill radius and corrected for gravitational focusing. **Bottom panel:** Only the exogenic grains are plotted (minimum velocity larger than the escape velocity, see text).

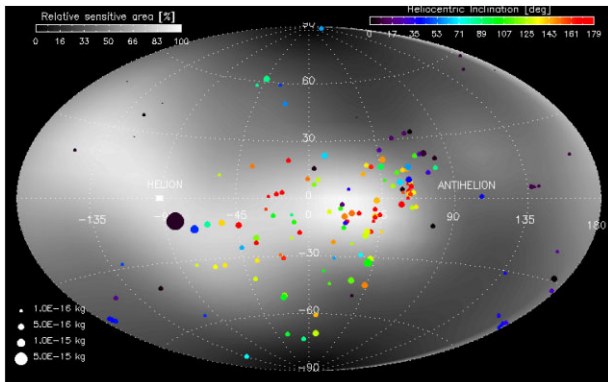


Figure 9. Longitude and latitude radiant directions at 1 RH of the CAT exogenic population in the SAT-APEX frame. The grey-scale indicates the integrated sensitive area of the CAT subsystem over Saturn's sky, when in measurement mode, during the entire mission. The Sun ('helion') and anti-Sun ('antihelion') directions are indicated in white.

The radiant directions at 1 RH of those exogenic particles are shown in Fig. 9. The entry points on the Hill sphere have been computed in a similar way than for the EG data, by backtracking the particles' trajectories, assuming the minimum impact speed

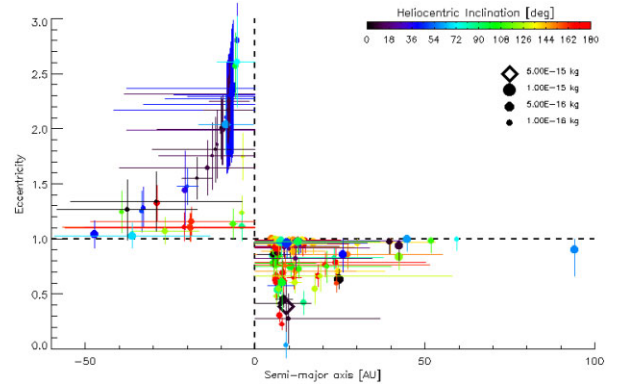


Figure 10. Heliocentric semimajor axis and eccentricities for all exogenic particles in the CAT data. The colour coding indicates the heliocentric inclination, and the symbol size is proportional to the particles' mass. The derivation of the error bar is explained in the text.

derived from the TOF analysis. Because the impact direction is only constrained by the aperture of the CAT field of view, the impact direction has been assumed to be along the instrument boresight. The grey-scale in Fig. 9 provides the time integrated sensitive area of the CAT subsystem during the entire mission over Saturn's sky.

In contrast to the EG subsystem, the CAT detector does not permit a direct retrieval of the particle radius. Instead, we derive a maximum mass value for each particle using the minimum impact speed and the ion charge yield (qi) generated upon impact, using the CAT calibration law (velocities v in km s^{-1} and masses m in kg).

$$\log(m) = -4.15 + 0.558 * \log(qi) - 5.59 * \log(v) - 0.144 * \log(v) * \log(qi). \quad (1)$$

While this approach is uncertain in determining the mass of an individual particle (because of the uncertainty on the impact velocity determination), the relative mass distribution is not affected. We plot in Fig. 10 the heliocentric eccentricities and semimajor axis distributions for all IDP particles detected by CAT, colour coded by heliocentric inclination, with the symbol sizes being indicative of the particles' mass. The error bars are inferred for each particle from all possible impact velocity vectors and their corresponding back-propagated trajectory to Saturn's Hill's radius. The orbital elements' standard deviation is derived, using as 'weight' for each solution the CAT sensitive area given by the angle between the impact direction and the instrument's boresight. For some grains, error bars in semimajor axis are very large (>50 au) and are in this case not plotted.

The CAT IDP (i.e. bound to the Sun) particles appear to have dominantly retrograde orbits (heliocentric inclination $>90^\circ$), with most of those particles' detections being distributed around Saturn's apex direction (Fig. 9). A population of grains unbound to the Sun also exists, on both prograde and retrograde hyperbolic orbits. We note that a significant number of grains have heliocentric eccentricity values close to unity (>0.9), on retrograde and prograde orbits. Considering the uncertainty of the impact velocity determination, which provides only a lower limit value of the impact speed (as explained at the beginning of this section), it is very likely that those grains are in fact unbound to the Sun, on prograde and retrograde hyperbolic orbits with low eccentricity.

The injection speed distribution of all CAT exogenic particles is plotted in Fig. 11, as well as the distribution for the heliocentric prograde and retrograde particles. Most particles have fast injection

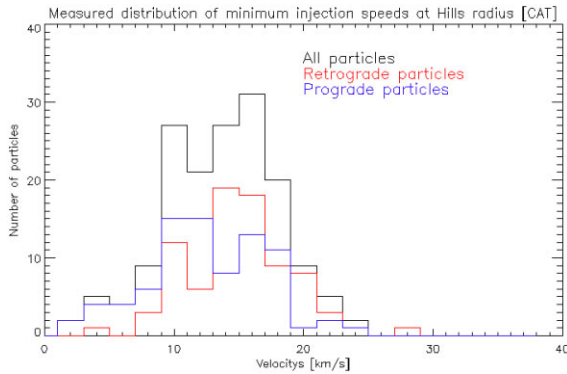


Figure 11. Minimum values of the injection speed distribution at 1 RH of the exogenic CAT particles. The black line is the distribution for all particles, while the blue and red lines stand for the heliocentric prograde and retrograde orbits, respectively.

speeds (over 10 km s^{-1}). Slow ($< 10 \text{ km s}^{-1}$) particles are in minority and dominated by prograde particles, while the retrograde particles have the peak of their minimum injection's speed distribution around 15 km s^{-1} .

3.3 Impact ionization detector data

The analysis of the IID data requires a different approach compared to the analysis of the EG and CAT detector data. The IID subsystem provides only coarse dynamical information for impacting grains, such that detections on the IID subsystem do not yield sufficient constraints on the particles' orbital elements to unambiguously identify exogenic particles. However, the IID detector, being sensitive to a wider range of particle sizes (10^{-15} to 10^{-9} g for impact speeds ranging from 2 to 40 km s^{-1} ; Srama et al. 2004) and having a larger aperture ($\pm 45^\circ$) than the CAT subsystem, provides much better statistics than the CAT and EG subsystems. In particular, the analysis of the IID impact frequency and their distribution in the Saturnian system can provide information on the contributing dust populations to the total flux. We follow an approach similar to the one used by Krivov et al. (2002) to characterize the Jovian dust populations measured by the dust detector onboard the *Galileo* spacecraft. Our observable for this analysis is the impactors' detection frequency as function of the radial distance to Saturn. The observed distribution is then modelled as a superposition of the different exogenic dust populations (whose existence in the Saturnian system is already proven by our analysis of the EG and CAT data), with the aim of constraining their relative abundances.

A key point and a prerequisite to estimate the contribution of various exogenic dust particles in the IID data set is to filter out noise events and the contribution of the E ring particles as conservatively as possible. The filtering steps are explained in detail in the next paragraphs.

3.3.1 Identification of genuine dust impacts

We followed strictly the 'coincidence criterion' used for IIDs (Grün et al. 1995) to reduce noise events. An event was considered to be a genuine dust impact if at least one channel (the electron channels of the chemical analyzer target QC and of the impact ionization target QT, or the multiplier channel MP; see Srama et al. 2004 for details) was triggered in addition to the QI channel (positive ions). In order to filter as much as possible numerous additional faint noise events not

removed by the coincidence criterion, we selected only impactors with ion impact charge higher than 5 fC. This criterion has also the advantage to filter out the tiny Saturnian 'stream particles' that produce in general less than 3 fC ion charge (Hsu et al. 2011).

3.3.2 Filtering of E ring contribution

E ring particles are filtered from our data set as conservatively as possible by rejecting all detections made in regions of the Saturnian system where the abundance of E ring particles is expected to exceed largely the abundance of exogenic populations. The zones of exclusion are defined by their ranges in radial distance to Saturn and vertical distance to the ring plane. We based our selection criteria on the most recent E ring observations and modelling.

The *Cassini* mission has demonstrated that E ring particles are produced by the cryo-volcanic activity of Enceladus (Spahn et al. 2006a, b). The large-scale structure of the E ring was characterized in detail by *in situ* CDA measurements (Kempf et al. 2008; Postberg et al. 2008; Srama et al. 2011; Linti et al. 2024b), by remote sensing observations (Showalter, Cuzzi & Larson 1991; Hedman et al. 2012), and modelling (Horányi, Juhász & Morfill 2008). The E ring has been shown to extend radially up to Titan's orbit and beyond, with a particle number density that decreases with increasing radial distance following roughly a steep power law. The abundance of E ring particles beyond Titan's orbit seems to be low enough and well concentrated within the ring plane, such that we did not exclude any region of space beyond Titan's orbit for our data set filtering. Within Titan's orbit, however, the situation is less favourable, with E ring particles expected abundantly within and above the ring plane. The E ring vertical structure, for particles as small as $0.1 \mu\text{m}$, has been observed using optical measurements at visible wavelengths to extend up to 1 RS above the ring plane (Showalter et al. 1991; Hedman et al. 2012). Even smaller particles, originating from the main ring system, lifted electrostatically and able to trigger an ion impact charge as high as 100 fC, have been detected *in situ* beyond 1 RS to the ring plane during the so-called Ring Grazing and Grand Finale Orbits of the *Cassini* mission (Hsu et al. 2018; Linti et al. 2024b). Non-icy, silicate material has been observed well above the ring plane (Linti et al. 2024b), ejected from the main rings by micro-meteoroid impacts. We therefore aimed at rejecting detections made at those high-latitude regions, while keeping sufficient statistics in the overall data set. We explain in the next paragraphs how the selection criteria were chosen for the regions of space within Titan's orbit.

In Fig. 12, we study the radial abundance profiles of all IID particle detections for different constraints on the distance to the ring plane (applied only within Titan's orbit). The different plot panels show the profile obtained by rejecting from the data set any dust detection occurring below a vertical distance to the ring plane of 1, 3, 6, and 8 RS. The grain abundance is defined by dividing the number of particle detections that occurred within each distance bin by the total spherical volume centred on Saturn and enclosed between the bin distance boundaries, and by the total time spent by the spacecraft within this volume. We observe a sharp increase in grain abundance closer to Saturn (note the logarithmic scale), even at a few RS above the ring plane, with abundances higher by orders of magnitude compared to the values obtained beyond Titan's orbit. Considering that the strength of the gravitational focusing effect at Saturn (Fig. 13), for exogenic particles injected at the Hill boundary, cannot explain such a strong abundance enhancement, even in the most favourable injection conditions, we conclude that most of the

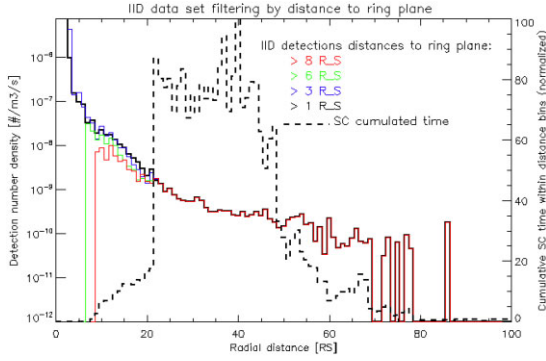


Figure 12. Distribution of the number density of IID detections as function of the radial distance to Saturn (plain coloured lines). The cumulative time spent in each distance bin by the spacecraft is represented by the dashed line. The number density of detections is obtained by dividing the number of detections in each distance bin by the product of the total time spent by the spacecraft in each bin with the volume of space delimited by the spheres centred on Saturn and having radii equal to the upper and lower bin boundaries.

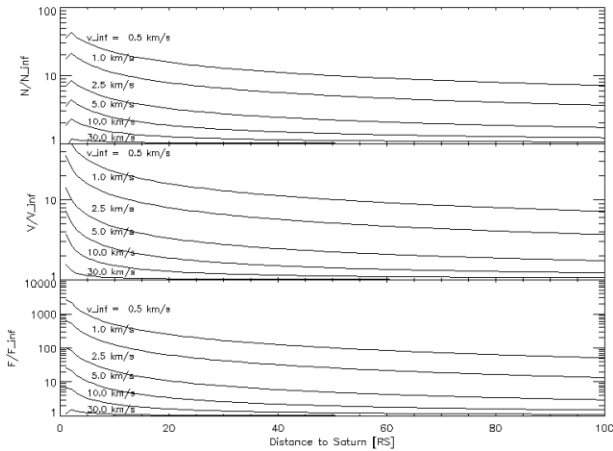


Figure 13. Gravitational focusing at Saturn for different values of injection velocities into Saturn’s Hill’s sphere. The upper panel shows the increase in volume number density, the middle panel shows the acceleration of grains, and the lower panel shows the resulting combined effect on flux.

particles detected within Titan’s orbit, and up to at least 6–8 RS vertical distance to the ring plane, are particles gravitationally bound to Saturn. We therefore conservatively filter our data set by removing any detection performed within 8 RS vertical distance to the ring plane and 22 RS radial distance. While we do not investigate further the bound particles able to reach such large distances above the ring plane, we note that their detection suggests the existence of an extended dust halo, not seen so far by remote sensing observations. Their origin and orbital evolution remain to be explained. Beyond the orbit of Titan, following the results of Horányi et al. (2008) and Kempf et al. (2008), we expect the E ring particles to remain relatively close to Saturn’s equatorial plane, and we conservatively reject all detections made within 2 RS of the ring plane.

The distribution of the filtered data set in the Saturnian system is shown in Fig. 14, together with the cumulative time spent by *Cassini* in each distance bin (taking into account only those time periods when CDA was in measurement mode, able to acquire IID data). This plot illustrates that, following our selection criteria to reject

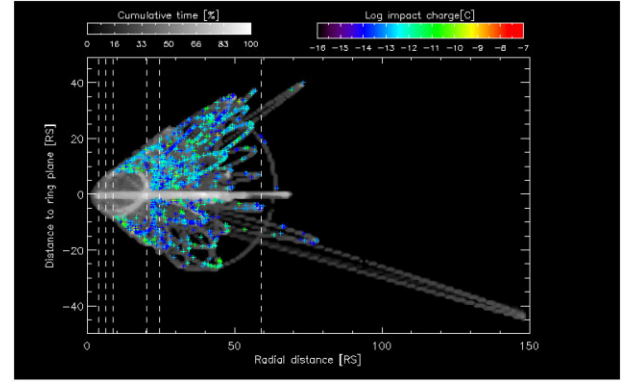


Figure 14. IID dust impacts used for the modelling of the exogenic dust relative contributions (see text). The grey-scale indicates the relative time spent by *Cassini* in the radial distance/distance to ring plane bins. The colour of the individual dust detection points scales with the total ion amplitude generated upon impact on the IID target. The vertical dashed lines indicate the orbits of Enceladus, Dione, Rhea, Titan, Hyperion, and Iapetus.

contributions from E ring particles, only those impacts were kept that were detected in high-latitude regions (8 RS distance from the ring plane) within Titan’s orbit. Beyond Titan’s orbit, particles were detected up to 40 RS distance from the ring plane, while detections made within 2 RS of the ring plane were rejected. This data set will be used as our observable for the modelling of the IID data presented in Section 4.5.

4 MODELLING

Modelling is performed on the data sets obtained by the different CDA subsystems presented in Section 3. The measurables to be modelled are the grains’ injection speed distribution, their radiant direction, and their heliocentric orbital elements, as well as the relative abundance of the different populations. We review briefly in Section 4.1 the characteristics of possible dust sources in the outer Solar system as currently known, before using this knowledge to model the EG and CAT data in Section 4.2 (injection speeds), Section 4.3 (radiant directions), Section 4.4 (orbital elements), and IID data in Section 4.5 (relative abundance using the detections’ radial distribution).

4.1 Interplanetary dust populations’ sources in the outer Solar system

4.1.1 Jupiter-family comets

A major source of dust in the outer Solar system are the JFCs, which are short-period comets known to be prolific dust producers in the outer Solar system. Theoretical work by Nesvorný et al. (2010) suggests that these comets could even be the dominant source of dust grains at larger heliocentric distances. For these comets, dust release occurs mainly upon disruptions induced by thermal stress, rotational splitting, or internal gas pressure variations (Weissman 1980; Bohnhardt 2004), rather than sublimation of volatiles. Recent studies show that, while the rate of JFC splitting events decreases slowly with increasing heliocentric distance, the spatial density of JFC is slowly increasing, resulting in a dust production rate that should be roughly independent of heliocentric distance (di Sisto, Fernández & Brunini 2009). The dynamics of JFC grains are mainly driven by solar gravity with strong perturbations from

radiation pressure and Jupiter encounters. Large grains (millimetres to centimetres) are found on trail structures that diffuse slowly in the orbital element space over time (Sykes et al. 1986; Levasseur-Regourd et al. 2018). Sub-micrometre- and micrometre-sized grains (within the sensitivity range of *Cassini* CDA) are dispersed rapidly by radiation pressure.

4.1.2 Kuiper belt objects

Dust can be released by collisional processes between KBO parent bodies (Stern 1996) or by erosion of a surface upon impact with interstellar grains (Yamamoto & Mukai 1998). The transport of KBO dust towards the inner Solar system has been studied theoretically by Liou, Zook & Dermott (1996), Moro-Martín & Malhotra (2002), Poppe & Horányi (2012), and Poppe (2016). It shows that up to 20 per cent of the grains in the 1–9 μm size range can spiral down to the Sun under Poynting–Robertson drag, while 80 per cent get trapped by mean motion resonances between the giant planets or are scattered. The time-scale for a dust grain to migrate from the Kuiper belt down to Saturn’s orbit is size dependent, but of the order of a few Myr for micron-sized grains (Liou et al. 1996).

4.1.3 Centaurs

Centaurs are considered as dynamically recently evolved objects from the Kuiper belt, probably representing an intermediate class of objects before their transition to JFCs if they are not ejected from the Solar system by gravitational scattering upon encounter with the giant planets. So-called active Centaurs are those objects that display a cometary-like activity despite their location far beyond the orbit of Jupiter, preventing a cometary activity driven by water sublimation (Jewitt 2009a). Some Centaurs have been shown to release as much dust as ‘traditional’ comets around their perihelion (Epifani et al. 2011). However, the number of Centaurs known to display a cometary activity is by far smaller than in the case of the JFCs, but they are harder to observe and their number is growing as more observation programmes are initiated. Centaurs are found between the orbits of Saturn and Neptune. Active Centaurs could therefore provide a source of ‘fresh’ dust at Saturn, having spent less time in the interplanetary space than the grains released from the more distant sources such as the Edgeworth–Kuiper belt (EKB) or JFCs (Poppe 2019).

4.1.4 Oort cloud comets

Oort cloud comets (OCCs) such as Hale-Bopp are very long period or long-period comets, believed to originate from the Oort cloud reservoir (Wang & Brasser 2014). They have broad inclination distributions, high eccentricities, and are the main source of heliocentric retrograde dust particles (heliocentric inclination larger than 90°). Those bodies become active once they enter the inner Solar system and release dust upon disruptions due to the build-up of thermal gradients, volatile phase transition, and pressure increase (Nesvorný et al. 2011). Overall, retrograde populations released by OCCs were shown to contribute by less than 10 per cent to the zodiacal cloud brightness, using different models and calibration methods (Nesvorný et al. 2010; Pokorný et al. 2014). However, recent studies have demonstrated that retrograde IDPs are one of the dominant producers of ejecta on the lunar surface and on the surface of asteroids near 1 au (Szalay & Horányi 2015, 2016). The *Pioneer 10* dust detector data revealed that this population, albeit

less abundant at 10 au than the dust grains originating from KBOs and JFCs, is required to explain the measurements of dust volume number density (Landgraf et al. 2002; Poppe 2016).

4.1.5 Haley-type comets

Haley-type comets (HTCs), with orbital periods ranging from 20 to 200 yr, can be the parent bodies of dust populations with high eccentricities and retrograde orbits. However, we mention HTCs for completeness only and we do not consider them further in this study, as they are not expected to be a significant dust producer at Saturn’s heliocentric distance, with grain abundance concentrated in the inner Solar system (Poppe 2016) for an overall <1 per cent contribution to the interplanetary dust flux (Nesvorný et al. 2010).

4.2 Modelling of the injection speeds’ distribution

The analysis of the EG and CAT data performed in Sections 3.1 and 3.2 shows the existence of particles with low or fast injection speeds at 1 RH (peaking at 4–5 km s^{-1} for the slow particles and at 18–20 km s^{-1} for the fast ones). Fig. 15 shows the injection speed distributions derived from the two subsystems, normalized to their maximum in order to better compare their respective velocity range and maxima. Overall, the EG data appear to have more slow particles with a narrower distribution than the CAT data.

The heliocentric orbits of particles with diameter 0.5, 1, 2, and 10 μm , injected into the Solar system by OCCs, JFCs, and EKBs, have been integrated using the simulations as described in Poppe (2016), in order to estimate their injection velocity at Saturn. The resulting distributions (normalized to their maximum such as to empathize their peak location) are shown in Fig. 15 as coloured overlay on top of the EG and CAT distributions. The theoretical distributions of the injection speeds, in particular their peak location, show some weak dependence on the particle size. The theoretical injection speeds of JFCs and EKB grains in the 1–2 micron size range at about 4–5 km s^{-1} correspond best to the peak of the injection speeds’ distribution derived from the EG data (Fig. 4), suggesting that those populations dominate the EG data set. While JFC and EKB dust particles appear, in terms of injection speed, to be a good match with the slow IDPs in the EG data, OCC dust is the only IDP population that can explain the fast IDPs.

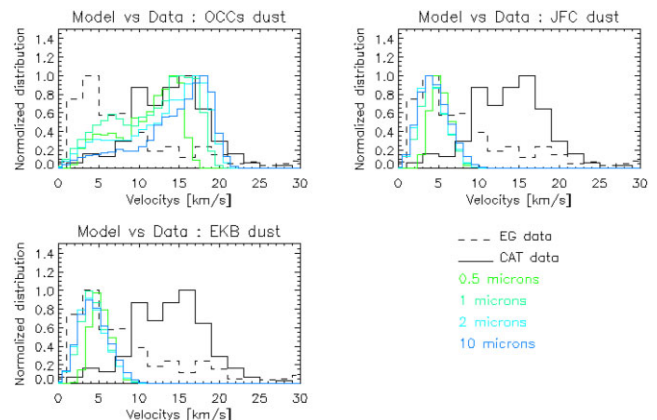


Figure 15. Normalized distributions of the injection speeds at the Hill sphere of Saturn of the exogenic EG particles (dashed line) and CAT exogenic particles (plain line), compared to simulations of grains from OCC, JFC, and EKB origin.

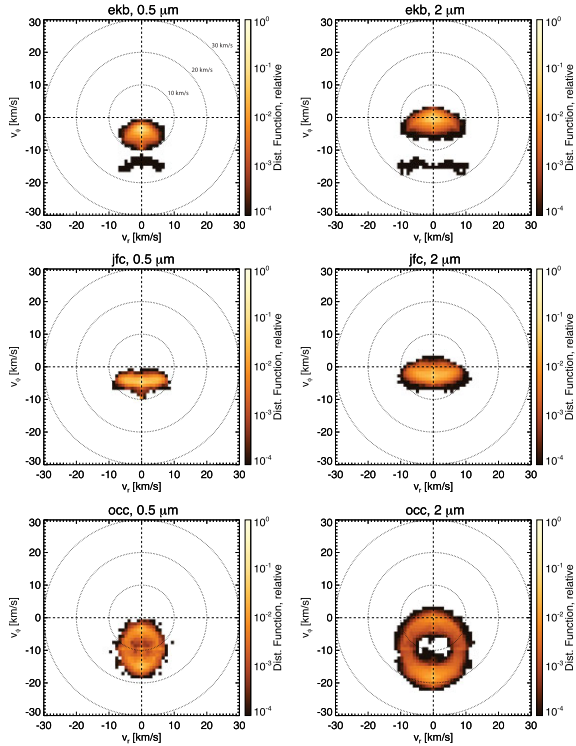


Figure 16. Modelled distribution (relative frequency) of EKB, JFC, and OCC particles, as function of their radial v_r and tangential v_ϕ components of their velocity relative to Saturn. $v_\phi > 0$ corresponds to the direction of motion of Saturn, and $v_r > 0$ corresponds to the anti-Sun side of Saturn’s orbit.

Smaller OCC grains (which comprise grains smaller than 1 micron) are in reasonable agreement with the main broad peak of the CAT data although there seems to be a deficit of detections with CAT below 10 km s^{-1} , possibly due to a reduced detection sensitivity in the lower speed regime.

4.3 Modelling of the radiant directions

The velocity vectors of OCC, JFC, and EKB grains on their heliocentric orbits as they reach Saturn have been modelled (for details, see Poppe 2016) and the results are summarized in Fig. 16.

The plots indicate the distribution (relative frequency) of the particles, in terms of their radial v_r and tangential v_ϕ components of their velocity relative to Saturn. Hence, the y-axis of those plots indicates whether the grains will preferentially come from the apex ($v_\phi < 0$, that is, Saturn is ‘catching up’ with the grains), or from the anti-apex direction ($v_\phi > 0$ if the grains are ‘catching up’ with Saturn). Low (respectively high) absolute values of v_r and v_ϕ indicate particles having low (respectively high) velocities relative to Saturn. In addition, the v_r values indicate the tendency of the particles to come from the Sunward ($v_r < 0$) or anti-Sunward ($v_r > 0$) directions of Saturn’s orbit. Considering the logarithmic scale of the frequency distribution, the model shows that larger grains ($2 \text{ }\mu\text{m}$) have predominantly lower injection speeds at Saturn. The model also predicts that large IDP grains of EKB and JFC origin have both an apex and anti-apex component, while small sub-micron EKB and JFC grains will have only an apex component. In all cases, the spreads in radial direction extend symmetrically towards the Sun and anti-Sun directions. Most of the OCC grains are

predicted to have high injection’s speeds and to have mainly an apex component, with a symmetric spread of their radiants towards the Sun and anti-Sun directions. Note that the vertical component of the injection velocities (due to the inclination of the grains’ trajectories with respect to Saturn’s orbital plane) is not shown in Fig. 16 but modelled and discussed separately in Section 4.4.

Comparing the theoretical radial and tangential components of the injection velocities with Fig. 7, we see that the distributions of the IDP grains detected by the EG subsystem (grains with radii larger than $1 \text{ }\mu\text{m}$, slow, heliocentric prograde populations) have radiants with both an apex and anti-apex component, in agreement with the model results for large JFC and EKB grains. In turn, the fast IDP population detected by the CAT subsystem has a radiant direction towards the apex direction only, with a wide spread of a few tens of degrees towards the solar and anti-solar directions (Fig. 9). This behaviour is qualitatively and quantitatively expected from modelling for the OCC grains. In particular, considering the simulated $0.5 \text{ }\mu\text{m}$ grains (most representative of the typical grain size detected by CAT), the maximum offset from the apex direction can be estimated from the grains having a maximum value of the radial component of $|v_r|$ up to $6\text{--}7 \text{ km s}^{-1}$ combined with a tangential component value of $|v_\phi| \approx 10 \text{ km s}^{-1}$, yielding an expected offset of the radiant from the apex direction of about 30° . This maximum offset appears in good agreement with our data towards the Sun direction (Fig. 7). The apparent asymmetry of the CAT particle detections, extending towards the anti-Sun direction beyond 45° from Saturn’s apex, is compatible with the additional 28° of the CAT half aperture angle combined with the comparatively larger integration time towards the anti-Sun direction than towards the Sun direction (Fig. 9).

This comparison of the modelled-versus-observed radiant directions of the grains would therefore support a possible OCC origin for the fast IDPs, including a contribution of ISD, while JFC and EKB grains can explain the observed radiant directions of the slow IDPs.

4.4 Modelling the heliocentric orbital elements

Further constraints on the origin of the IDP particles detected by CDA at Saturn can be derived from a comparison of their heliocentric orbital elements as presented in Section 3 with the ones derived from modelling. The details of the model used to perform these simulations for JFC, EKB, and OCC particles are described in Poppe (2016). We discuss in the next paragraphs the compatibility of the different possible dust sources with the heliocentric orbital elements derived from the EG and CAT subsystems. The comparisons of the orbital elements of the detected dust grains (values of the heliocentric semimajor axis, eccentricity, and inclination) with simulated grains from EKB, JFCs, and OCC origin are shown in Figs 17 and 18 for the EG and CAT subsystem data.

4.4.1 Dust from EKB

Most of the simulated grains have low to moderate eccentricity and low inclination values when they reach Saturn’s orbital distance and are therefore good candidates for the large, micron-sized IDP component (detected by the EG subsystem), with low injection speed at Saturn’s Hill’s radius. The grains measured by the EG detector with low inclinations, a semimajor axis larger than 10 au but moderate eccentricities, are also well explained by the simulated EKB grains.

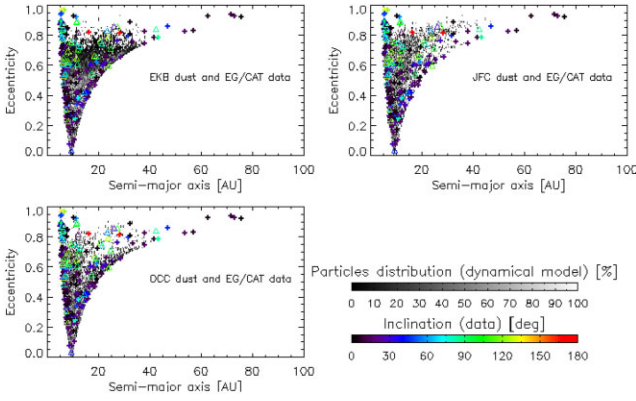


Figure 17. Distribution of the semimajor axis and eccentricity of the Sun-bound IDP particles detected by the EG (cross symbols) and CAT (triangle symbols) subsystems, colour coded as function of their inclinations. The modelled distributions for 2-micron-sized grains of EKB, JFC, and OCC origin are given by the black dots in the top left, right, and bottom left panels, respectively. The grey-scale indicates the relative abundance at 10 au of the simulated particles.

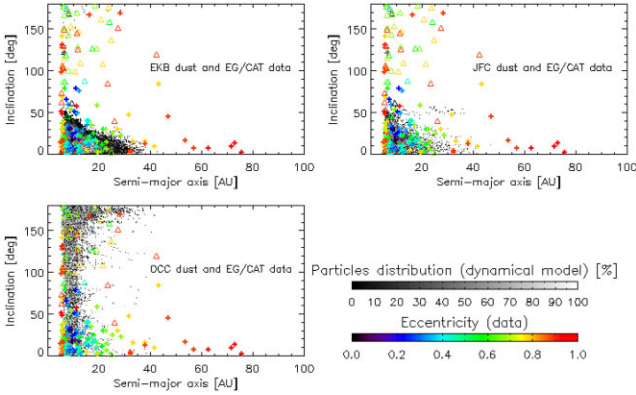


Figure 18. Distribution of the semimajor axis and inclination of the Sun-bound IDP particles detected by the EG (cross symbols) and CAT (triangle symbols) subsystems, colour coded as function of their eccentricities. The modelled distributions for 2-micron-sized grains of EKB, JFC, and OCC origin are given by the dots in the top left, right, and bottom left panels, respectively. The grey-scale indicates the relative abundance at 10 au of the simulated particles.

4.4.2 Dust from JFC

Particles released by JFCs are similar to the EKB particles also concentrated within a few tens of degrees from the ecliptic plane. The eccentricities at Saturn of JFC grains are low to moderate, but, opposite to the EKB grains, there is no dominant component on nearly circular orbits at 10 au, and no dominant component with a semimajor axis larger than 10 au. The majority of the particles have eccentricities ranging from 0.3 to 0.6, with a semimajor axis around 7 au. Those values match well the semimajor axis and eccentricity values of many EG particles with low inclinations.

4.4.3 Dust from Centaurs

We also analysed analytically the dynamical signature of dust grains released by Centaurs at Saturn’s heliocentric distance. Considering that active Centaurs provide dust sources close to Saturn’s orbit, this approach allows us to derive heliocentric orbital elements of grains

recently released by their parent bodies, considering solar radiation pressure as the main parameter affecting the grains’ dynamics, without having to model the trajectory evolution over long period of times, as we have done for grains from remote sources such as JFCs and KBOs. We summarize in what follows the modelling of the dynamical signature at Saturn of grains originating from Centaurs.

We assume a dust grain released with the velocity vector \mathbf{v} from the parent comet body at a heliocentric distance \mathbf{r} . The additional velocity provided by the dust ejection process (typically a few hundred metres per second) is only a tiny fraction of the parent body velocity with respect to the Sun and can therefore be neglected. We call the ratio between radiation pressure and gravity the β -ratio (Burns, Lamy & Soter 1979). Writing conservation of energy per mass unit for the grain $\frac{v^2}{2} - \frac{\mu}{r} = -\frac{\tilde{\mu}}{2\tilde{a}}$ and the parent body $\frac{v^2}{2} - \frac{\mu}{r} = -\frac{\mu}{2a}$, with $\tilde{\mu} = (1 - \beta)\mu$, and applying the velocity condition at injection $\mathbf{v} = \tilde{\mathbf{v}}$ at the position \mathbf{r} yield

$$\tilde{a} = \frac{a(1 - \beta)}{1 - 2\frac{a}{r}\beta}, \quad (2)$$

where a and \tilde{a} are the semimajor axes of the parent body and the dust particle, respectively. Furthermore, the angular momentum per mass unit of the parent body and of the released dust grain are identical, such that we can write $\mu a(1 - e^2) = \tilde{\mu} \tilde{a}(1 - \tilde{e}^2)$ and using (2) we find

$$\tilde{e} = \sqrt{1 - \frac{(1 - e^2)(1 - \frac{2a\beta}{r})}{(1 - \beta)^2}}, \quad (3)$$

where e and \tilde{e} are the eccentricities of the parent body and the dust particle.

A numerical application for 29P/Schwassmann–Wachmann 1 (SW1) ($a = 6.25$ au, $e = 0.04$, known as a comet but matching the dynamical definition of a Centaur; Jewitt 2009a) using equation (3) shows that Centaur grains can have low to moderate heliocentric eccentricities (and hence will have low injection speed at Saturn’s Hill’s radius), if their β values are sufficiently small (practically $\beta \leq 0.2$). Their heliocentric eccentricity increases then sharply with increasing β values up to the limit of $\beta \approx 0.5$ where no bound heliocentric orbit can be maintained, such that particles released by the parent body leave the Solar system on hyperbolic trajectories.

Fig. 19 shows all identified Centaurs (cross symbols, with active Centaurs are highlighted in black) from the Jet Propulsion Laboratory (JPL) ‘Small Bodies Database’ (<http://ssd.jpl.nasa.gov/sbdb.cgi>) in (a, e) plots. Starting from each Centaur, using equations (2) and (3), we draw a dashed line representing all the positions in the diagram [its (a, e) values] that a dust grain can have, depending on its β value, after being released from the Centaur’s surface. The EG exogenic solutions are plotted on top as circles, whose radii are proportional to the logarithm of the grains’ radius, while the colour coding indicates the inclination. The top panel shows the grains on solar bound orbits, and the bottom panel shows all EG grains including the particles on solar hyperbolic orbits. Interestingly, active Centaurs appear to be a plausible source for the detected solar bound *prograde* particles, with low semimajor axis values and low to medium eccentricities, or with larger semimajor axis and high eccentricities. For the *prograde* particles on hyperbolic solar trajectories as well do the Centaur hypothesis provide a good match, with the particles located on the dashed lines corresponding to $\beta > 0.5$. In the micron-size range covered by the EG detector, the β ratio increases as the particle size decreases. The smaller particles released by Centaurs would therefore be more likely than larger ones to be blown out of the Solar system by radiation pressure on hyperbolic orbits. This is in

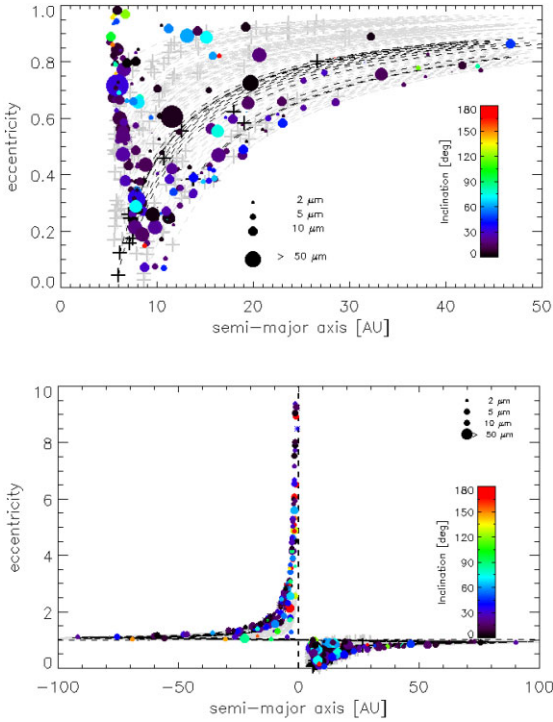


Figure 19. Distribution of the semimajor axis and eccentricity of the particles (coloured circles) detected by the EG detector, for both solar bound and unbound solutions (bottom panel) and for the solar bound solutions only (top panel). The semimajor axis and eccentricity of known Centaurs (as per JPL small body data base) are indicated by the crosses, the black crosses standing for object with recorded cometary activity. The loci of dust particles ejected by those parent bodies are indicated by the dashed lines for β values ranging from 0 to 1.5 (see Section 4.4.3).

qualitative agreement with the fact that we find only small grains on hyperbolic orbits in Fig. 19, bottom panel.

So far, we have shown that EKB objects, JFCs, and Centaurs can explain the origin of Sun-bound and Sun-unbound prograde IDPs at Saturn, with the Sun-bound particles being the main component of the slow IDPs entering Saturn’s Hill’s sphere. However, none of those sources can provide a satisfactory explanation for particles with high inclinations and/or high eccentricities (prograde and retrograde), resulting in higher relative velocities with the planet. The following paragraphs discuss a possible origin for fast particles.

4.4.4 Dust from OCCs

Owing to their wide distributions in heliocentric eccentricities and inclinations, OCCs are the most natural dust sources to explain the highly inclined (including retrograde), solar bound particles detected by the EG and CAT subsystems. Those highly inclined grains have higher relative speeds with Saturn than the prograde EKB and JFC grains and therefore provide an explanation for the fast IDP component at Saturn. The modelled distributions of semimajor axes, eccentricities, and inclinations of grains from OCCs and the distributions derived for the CAT IDP data are shown in the bottom panels of Figs 17 and 18. Note that the IDP data set is built from all exogenic grains in the CAT data that have a heliocentric eccentricity lower than 0.9 to avoid including particles that could be ISD grains, within the CAT measurement uncertainties. While the (a, e) distribution for OCC grains is quite similar to the ones for EKB and JFC particles, the main difference resides in the nearly uniform

distribution of inclinations ranging from 0 to 180°, a behaviour that the CAT data set also displays for solar bound particles. This suggests that a large fraction of the CAT solar bound grains, as well as the few EG grains with highly inclined orbits, come from OCC sources.

At this point, the modelling of the EG and CAT subsystem data supports the idea that the slow IDP population at Saturn is made of a mix of grains on heliocentric bound orbits with low to medium eccentricities that have been released by EKB, JFCs, and Centaur sources.

The fast IDP population, in turn, may be provided by OCC sources. We aim in the next section at deriving the relative abundance of the slow and fast IDP populations, using a statistical analysis of the IID subsystem data.

4.5 Relative abundance of the fast and slow IDP populations – modelling of the IID data

In this section, we model the distribution of the IID dust impacts, as derived in Section 3.3, to constrain the relative abundance at 1 RH of the different IDP populations at Saturn (whose existence has been established by the analysis of the EG and CAT data) and to constrain the total IDP and ISD relative abundance. We remind the reader that we do not attempt a direct assessment of whether a grain detected by the IID subsystem is on bound or unbound orbit around Saturn, because of the large uncertainty on the determination of the impact velocity vector (about a factor of 2 in speed and 45° in direction; Srama et al. 2004). The IID subsystem target area used in the computations is 0.086 m².

To model the IID impact distribution, we consider the slow IDPs, the fast IDPs, and ISD particles as possible contributors. Because the strength of gravitational focusing depends primarily on the particles’ injection speed v_∞ at the Hill boundary (see Fig. 13, based on the formula derived by Spahn et al. 2006a), we use the Saturn system as a giant velocity spectrometer that modulates the abundance of different exogenic dust populations at different radial distance to Saturn, depending on their injection speed. Indeed, as shown in Fig. 13, the slower the injection speed of the particles, the higher is the effect of flux enhancement through gravitational focusing with decreasing radial distance to Saturn (via an increase of both, volume number density and speed). In contrast, grains injected at higher speeds will have a volume number density and speed more independent of the radial distance to Saturn. The number of grains expected in each distance bin is computed for each population over the time covered by the IID data set, using the CDA’s pointing profile, the spacecraft position, and its velocity as a function of time, combined with the abundance, speed, and directionality of each population. Because the flow of ISD grains at Saturn is well constrained from previous work (Landgraf et al. 2003; Mann 2010; Sterken et al. 2012; Altobelli et al. 2016), as well as the average injection speeds of the slow and fast IDP populations from Sections 3 and 4.2, the number of grains detected per distance bin for the slow and fast IDP populations is ultimately parametrized by their volume number densities ($n_{\text{slow}}^\infty, n_{\text{fast}}^\infty$), respectively, at 1 RH. We apply a least-square fit method in order to find the values of ($n_{\text{slow}}^\infty, n_{\text{fast}}^\infty$) for which the detected numbers of slow and fast IDPs match best the observed radial distribution. We detail the computations and assumptions for each population in the next two paragraphs.

4.5.1 ISD

We assume for the ISD grains the dynamical model as described in Landgraf et al. (2003) and Sterken et al. (2012) and their

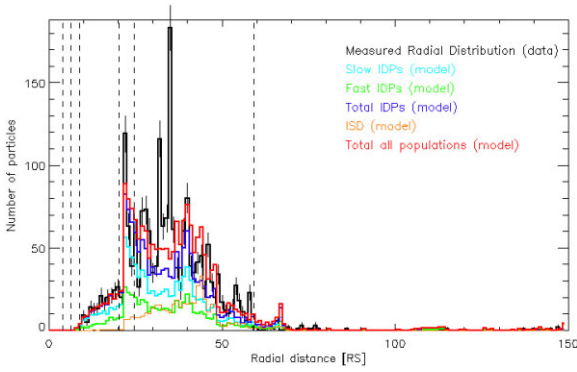


Figure 20. Distribution of IID impacts' detection as function of the radial distance to Saturn, after applying the selection criteria as described in Section 3.3. The fit of the measured distribution resulting from the computed frequency per distance bins of different dust populations (see Section 4.5) is shown by the coloured lines. The vertical lines indicate the orbital distance of (in order of increasing radial distance) Enceladus, Dione, Rhea, Titan, Hyperion, and Iapetus.

characterization at Saturn described in Altobelli et al. (2016). Those works provide us with the ISD injection direction and speed at Saturn and a flux value (upper limit) of $1.5 \times 10^{-4} \text{ m}^2 \text{ s}^{-1}$. The most abundant grain size in the ISD flow in the Solar system corresponds to a radiation pressure to gravity ratio of $\beta = 1.1$ (sub-micrometre grains with $\approx 0.3 \mu\text{m}$ radius for a density of 2500 kg m^{-3} assumed usually for so-called astronomical silicates; Love et al. 1994), which we use to infer the impact direction and speed of ISD grains along *Cassini's* trajectory. The angle between the pointing of CDA at the time of impact and the ISD grain impact direction constrains the IID effective sensitive area exposed to the flow. This geometrical sensitive area is additionally corrected to take into account the enhancement of the particle flux resulting from the spacecraft motion. The modelled number of ISD grain detections within each bin of distance is shown in Fig. 20. We observe that ISD grains alone cannot account by far for the observed radial distribution, although a significant contribution is expected between 20 and 50 RS. Note that gravitational focusing does not significantly alter the directionality nor the speed of ISD grains with respect to Saturn, owing to their relatively large injection speed.

4.5.2 IDPs

Considering the sensitivity of the IID detector, and the relative abundances of grain sizes naturally following a power law, the smaller, sub-micrometre-sized IDP particles must dominate our data set. Following the dynamical model predictions for sub-micrometre grains at Saturn and the analysis of the CAT and EG subsystem data (Figs 15 and 16), we assume slow (respectively fast) IDPs to be injected from the Saturn apex direction only, with an average entry speed relative to Saturn of 4 km s^{-1} (respectively 16 km s^{-1}). The volume number densities at 1 RH for the slow and fast populations (n_{slow}^{∞} and n_{fast}^{∞} , respectively) are free parameters in our simulation. Within each distance bin, we compute the particles' speed and volume number density enhancement resulting from gravitational focusing and taking the spacecraft velocity into account. From the instrument's commanding history, we excluded from the simulation the time periods when CDA could not perform IID measurements.

Modelling the impact direction of the slow and fast IDP grains in the spacecraft frame (needed to know the sensitive area of the

IID detector) is not easy considering the distribution of the grains' injection direction at the Hill sphere (Fig. 16), in addition to the deflection of the grains' flight directions within the gravitational field of Saturn. For our computations, we have followed the following simplified approach: for each time-step of the simulation, we consider slow or fast IDP detections possible if CDA was pointed within 45° from the theoretical impact direction in the spacecraft frame that a grain would have, if injected along the apex of Saturn, with the speed characteristic for its population.

Within our modelling assumptions, we find that the overall radial profile of IID detections is well reproduced by the combination of the IDP and ISD populations. Both slow and fast IDP populations must be present at Saturn, and a best fit is achieved if the volume number densities at infinity are $n_{\text{slow}}^{\infty} \approx 4 \times 10^{-8} \text{ m}^{-3}$ and $n_{\text{fast}}^{\infty} \approx 1 \times 10^{-8} \text{ m}^{-3}$.

5 DISCUSSION

Our analysis of the *Cassini* CDA data shows that the Saturn system is traversed by particles having speeds larger than the Saturn's escape velocity, hence gravitationally 'unbound' to Saturn. In particular, we observe that all sub-micron grains detected beyond the orbit of Titan (CAT data) are unbound, because their inferred minimum speed with respect to Saturn exceeds the planet's escape velocity (Fig. 8). Unbound particles are either leaving or entering the Saturn system. Considering the size regime of the data set analysed in this work (sub-micrometre to tens of micrometres grains), it is logical to assume that those grains come from outside the Saturn system (exogenic origin) because dust ejection mechanisms known from Jupiter and Saturn are expected to provide enough energy to escape only to nanometre-sized grains, so-called stream particles (Horanyi, Morfill & Gruen 1993; Graps et al. 2000; Kempf et al. 2005). Having established the existence of exogenic dust grains at Saturn, we then tried to constrain their possible origins and relative abundances.

Using the EG and CAT subsystem data, we first constrained the particles' speeds at Saturn's Hill's boundary (so called injection speed), their radiant directions as seen from Saturn, and their heliocentric orbital elements before entering the Saturn system. Two main injection speed regimes are suggested by this analysis, the so-called slow and fast populations. The fast component is dominant in the CAT data, containing only sub-micrometre-sized grains, while the slow component dominates the EG data set, where micrometre-sized grains are the most abundant. Most of the injection speeds derived for the CAT particles (we recall that those speeds are a minimum value inferred from the CAT TOF spectra) range from 10 to 20 km s^{-1} with a peak of the injection speed distribution at about 18 km s^{-1} (Fig. 11). The fact that those particles triggered the generation of a proper TOF signal on the CAT electronics implies that less than 2 pC impact charge was released. Within the uncertainties on the knowledge of the density of the silicate particles (2500 kg m^{-3} for low-density amorphous IDPs and up to 3.3 kg m^{-3} for the denser crystalline grains), we conclude that the slower (about 10 km s^{-1}) exogenic CAT particles cannot be larger than $1 \mu\text{m}$ equivalent radius and the faster ones (20 km s^{-1} and above) cannot be larger than $0.5 \mu\text{m}$.

5.1 ISD population

Among the sub-micrometre, fast population, particles unbound to the Sun are present, whose radiant directions at Saturn and injection speeds can be explained by ISD particles crossing the Solar system. This population has been already characterized in previous work

(Altobelli et al. 2016). It is noteworthy that the EG data also confirm for the first time the existence of large ($>2\ \mu\text{m}$) grains on heliocentric hyperbolic orbits, whose radiant directions at Saturn are also compatible with the ISD stream (Figs 6 and 7). The observation of such large interstellar grains is only possible using *in situ* detection methods when they cross our Solar system, because their optical depth in the interstellar medium is too low to be detected by astronomical methods (Mathis, Rumpl & Nordsieck 1977). The dust detector onboard the *Ulysses* spacecraft has detected ISD grains with masses up to $10^{-13}\ \text{kg}$ (corresponding to $2\ \mu\text{m}$ equivalent silicate spheres; Krüger et al. 2007). Larger ISD grains were not detected *in situ* by previous missions and only the EG subsystem sensitivity and the long observation baseline of the *Cassini* mission made those detections possible. Due to their large size, the trajectories of those ISD grains in the heliosphere should not be affected by solar radiation pressure nor by the interplanetary magnetic field, which dominate the dynamics of sub-micrometre-sized particles (Sterken et al. 2012). A more detailed analysis will be needed to determine the relative abundance of those large ISD grains compared to the smaller population.

Interestingly, a number of grain detections by the EG subsystem also suggests the existence of interstellar micrometre-sized dust grains not belonging to the ISD stream. While the ISD stream in the Solar system is caused by the motion of the Sun with respect to the Local Interstellar Cloud, other Galactic sources of ISD in the Solar system have been postulated in the past, such as debris-disc stars or interstellar asteroids and comets. Those postulates were supported to some extent by radar detections of large ($>20\ \mu\text{m}$) interstellar meteoroids entering the Earth's atmosphere (Taylor, Baggaley & Steel 1996; Baggaley 2000) and, more recently, by the discovery of the first confirmed interstellar interlopers 1I/Oumuamua and 2I/Borisov (Williams et al. 2017; Higuchi & Kokubo 2020). A more detailed analysis of the EG data will be conducted to understand better the origin of those detection events.

5.2 IDP populations

The exogenic particles on bound solar orbits (IDPs) can be separated into a fast and slow component, in relation to their injection speeds at Saturn. The slow IDP component is dominant in the EG data set (Fig. 15), while the fast component is dominant in the CAT data. Considering the CAT upper limit for impact charge of 2 pC, for impact speed as low as $5\ \text{km s}^{-1}$, the CAT subsystem should also be able to detect the micrometre-sized IDPs that dominate the EG data set. Statistically, however, it is not surprising to not observe this type of grains in the CAT data, because the collecting area of the CAT detector is about 100 times smaller than the collecting area of the EG subsystem. Considering that the EG subsystem detected over the *Cassini* mission lifetime only 73 grains that could with certainty be identified as exogenic (Kempf et al. 2023), CAT is therefore essentially statistically blind for the large IDP component.

5.2.1 Interpretation of the slow IDP population

The slow IDP population is characterized by a grain size distribution as reported in Kempf et al. (2023) with a peak at about $3\ \mu\text{m}$. This population is made of heliocentric prograde particles, with low to moderate heliocentric inclinations. We compared the derived radiant directions, injection speeds, and heliocentric orbital elements with those expected for dust grains at Saturn after being released by

various known sources and processes: the cometary activity of JFCs and Centaurs, as well as collisions of parent bodies (KBOs) in the outer Solar system, with a subsequent dynamical evolution caused by Poynting–Robertson drag (Section 4.1). The peak of the injection speeds for the slow IDPs is reproduced best by either JFC or EKB dust, with sizes ranging from 0.5 to $10\ \mu\text{m}$. There is no significant difference in injection speed within this size range (Fig. 15). The radiant directions for the large and slow IDPs show no clear trend for an apex or anti-apex component, which seems in agreement with the simulations of large JFC and EKB grains at Saturn (see 2 micron EKB and JFC grains' simulations in Fig. 16), while large OCC particles should have a pronounced apex component (2 micron OCC grains in Fig. 16). The heliocentric orbital elements inferred from the simulations also support JFCs and EKB grains as the main contributors to the EG data set, while the characteristics of the heliocentric inclinations exclude the OCC as the dominant source for the slow IDPs (Figs 17 and 18). It appears impossible, however, to find clear criteria from our data and modelling to separate the relative contribution of JFCs and EKBs to the slow IDP population at Saturn.

We modelled analytically the orbital element characteristics of grains released by Centaurs. Those small bodies are dynamically evolved KBOs that have left the Kuiper belt to populate the space between Jupiter and Neptune, before they may dynamically evolve to JFCs (Jewitt 2009b). Those bodies have been identified in the last decade as prolific sources of dust (Jewitt 2009b; Epifani et al. 2011; Chandler et al. 2020). We estimated the heliocentric semimajor axes and eccentricities of grains released by Centaurs at their perihelion, using a simplified dynamical model that parametrizes the grain sizes by the values of their solar pressure to solar gravity ratio (Section 4.4.3). Our analytical model shows (Fig. 19, top panel) that a subset of the EG particles with low to high heliocentric eccentricities and low inclinations can be explained by dust released from Centaurs, which are known to be active. Interestingly, we observe that Centaurs can also be a source of particles on hyperbolic, low-inclination orbits with respect to the Sun (hence leaving the Solar system), as seen in Fig. 19, bottom panel. Owing to the Sun's radiation pressure and the relatively large distance from the Sun, particles with β values larger than ≈ 0.5 have a positive orbital energy (negative semimajor axis, see Fig. 19, bottom panel) and will leave the Solar system. If one considers a physical model for cosmic dust grains as developed by Kimura, Mann & Jessberger (2003), this minimum value for β translates (roughly, considering the model uncertainties, in particular the particle's bulk density) into a maximum mass of $\approx 5 \times 10^{-15}\ \text{kg}$ for this type of hyperbolic grains. This implies a $1\ \mu\text{m}$ equivalent diameter for the astronomical silicate density of $2500\ \text{kg m}^{-3}$ (see, for example, Sterken et al. 2012, their fig. 14, for an overview of the β -mass curves for different grain types). This grain size lies within the lower range of the EG detector's sensitivity, explaining why they could be detected.

We conclude from the discussion in the last two paragraphs that the primary source of slow IDPs at Saturn are KBOs or JFCs. Because JFCs are dynamically evolved KBOs (Lowry et al. 2008), the material from which the grains are made would therefore have the same origin, albeit with a different exposure history in the Solar system. In the KBO case, grains would have migrated towards Saturn after being released within the Kuiper belt and would have been exposed to the Sun's radiations and solar wind weathering for typically millions of years before reaching Saturn. In the JFC or Centaur hypothesis, the parent body itself would have first migrated towards the inner Solar system before releasing its (preserved) material upon sublimation or induced by thermal stress.

5.2.2 Interpretation of the fast IDP population

Fast IDP grains dominate the CAT data set but are also present in the EG data. In both subsystems, the fast IDPs appear as a population coming from the apex direction of Saturn with high heliocentric inclinations (heliocentric retrograde orbits) (Fig. 7). The minimum particle velocities with respect to Saturn derived from the CAT data are consistent with (after correction for the gravitational focusing) particles having injection speeds into the Saturn system ranging from 10 to 20 km s⁻¹ (Fig. 8). Only dust released from OCCs matches this preferential injection direction as well as this injection speed range (Fig. 15, upper left panel, and Fig. 16, bottom panels). It seems therefore reasonable to conclude that we detected dust from OCC objects with CDA. It must be noted, however, that Saturn's apex direction and the radiant direction of the ISD stream were close to each other in particular during the year 2009 (Sterken et al. 2012, their fig. 49). A detailed analysis of the grain composition, using the TOF spectra, will be carried out in a follow-up study, to identify differences between those two dust populations. It must be noted that OCC grains are *not* particles making their way from the Oort cloud reservoir to Saturn. They are produced within the Solar system during close encounters of their parent bodies with the Sun (Section 4.1). Having compositional information on such grains in the CAT data may allow us to provide new constraints on the different scenarios leading to the formation of the Oort cloud – either from scattered objects formed within the Solar system protoplanetary disc during planetary formation or by exchange of material with nearby stars (Zubrin 2020).

5.3 Relative abundance of different populations

We attempted to constrain the relative abundances of the different populations observed in the EG and CAT data set. To this aim, we used the IID data set, which, albeit not providing direct constraints on the orbital elements of individual particles, provides a large detection statistics and a sensitivity in grain size covering most of the CAT and EG sensitivity range (Section 3.3). The modelled observable related to the IID data set is the radial distribution of the number of particle detections, used to constrain the relative abundance of three populations: the fast and slow IDPs, and the ISD. To do so, we relied on the role of the gravity field of Saturn acting as a speed spectrometer, enhancing preferentially the abundance of particles with the slowest injection speeds with decreasing radial distances from the planet, while the abundance of the fastest particles remains unchanged (Fig. 13). We also took into account our prior knowledge on the directionality and particle abundance of the ISD stream. We then folded this information with the spacecraft velocity and pointing history of CDA and fitted the radial profile of the particle detections with the superposition of the three ISD and IDP populations. We then computed the number of particles expected to be detected by the IID subsystem, in each radial distance bin, parametrized by the population abundance at Saturn's Hill's radius, and assuming the bulk injection speeds and preferred radiant directions as inferred from the CAT and EG data analysis as well as from the dynamical modelling.

The total abundance of (fast and slow) IDPs derived in Section 4.5 is about 4–5 times higher compared to the IDP abundance derived from the SDC data acquired at 10 au, with an upper abundance limit of 10 particles per cubic km for a lower cut-off size of 0.63 μm (Doner et al. 2024). Considering that we may still have some contribution of particles bound to Saturn in our data set, our finding appears overall in very good agreement with the SDC analysis. We find the slow IDP populations to be about four times more abundant than the fast

populations at Saturn's Hill's radius, while Poppe (2016) suggests a similar abundance at 10 au, at least for the 2-μm-sized grains. Our result is, however, in good agreement with measurements performed by *Pioneer* (Landgraf et al. 2002) albeit in a different size regime.

In Fig. 20, we note the existence of dust detection peaks around 22, 32, 35, 40, 46, 49, 54, and 58 RS, for which our exogenic population mix does not provide a satisfactory explanation. Those particles are unlikely to be E ring particles, because of the filtering criteria applied to the IID data set (Section 3.3), but could still signify yet unknown particle populations bound to Saturn. The location of the peak within 22–25 RS, in particular, could be compatible with Hyperion as a potential source of the grains, as theoretically studied by Banaszekiewicz & Krivov (1997) and Krivov & Banaszekiewicz (2001). However, we note that all peaks contain clusters in detection times, even at large distances from the ring plane. Therefore, sporadic exogenic dust sources, such as dust trails or tails, could also be a possible explanation (Hedman et al. 2011; Krüger et al. 2020), but verifying this hypothesis is beyond the scope of this work. Beyond the orbit of Titan, more ISD grains are detected mainly because of the longer time dedicated to observation campaigns, performed by the spacecraft near its apocentres, pointing CDA towards the ISD radiant direction.

Because the abundance of the slow IDPs (such as dust from EKB, JFC, and Centaurs) is naturally enhanced by gravitational focusing, the slow IDPs are the most abundant exogenic dust population within Titan's orbit and are therefore a major contributor to the mass influx impacting the surface of the icy moons and of Saturn's rings (Poppe & Horányi 2012). Our finding has therefore consequences for studies on the understanding of the bombardment history, erosion, and alteration processes of the surfaces of Saturn's rings (Durisen 1984; Cuzzi & Durisen 1990; Durisen et al. 1992; Cuzzi & Estrada 1998; Durisen & Estrada 2023; Estrada & Durisen 2023; Kempf et al. 2023; Teodoro et al. 2023), and of Saturn's icy moons and ring moon system, where hypervelocity micro-meteoroid impacts play a key role, but where the only theoretical approach so far was an extrapolation to the outer Solar system of the knowledge of the dust populations at 1 au (Grün et al. 1985).

6 CONCLUSION

We have analysed the dust grains of exogenic origin detected by three *Cassini* CDA subsystems during the 14 yr spent by the mission in the Saturn system. The long mission baseline and the sensitivity of the instruments allowed the *Cassini* spacecraft to be an invaluable *in situ*, long-term monitoring platform of the interplanetary and ISD complex in the outer Solar system.

Our main findings are as follows:

- (i) The Saturn system is crossed by exogenic particles, of interplanetary and interstellar origin.
- (ii) The interplanetary dust population at Saturn is made of a mix of grains released from EKB objects, JFC, and OCC, as well as active Centaurs.
- (iii) The dust grains from EKB, JFC, and Centaurs have lower injection speeds (slow IDPs) at Saturn than the OCC grains (fast IDPs). While the relative abundance of the slow and fast populations at Saturn's Hill's radius is comparable, the slow IDP populations are more gravitationally enhanced, and therefore are more abundant within the Saturn system. EKB, JFC, and Centaur dust may therefore contribute comparatively more to the weathering of Saturn system objects than dust from OCCs.

(iv) A population of large ISD grains (micrometre-sized regime) is observed at Saturn, larger than those detected by previous *in situ* dust detectors.

(v) Large ISD particles are detected, which do not seem to belong to the ISD stream.

(vi) Unexpected high numbers, often clustered in time, of grain detections above the modelled exogenic background are registered at large distances (>3 RS) above the ring plane within narrow distance bins to Saturn. It remains to be investigated whether those detections are related to endogenic dust sources or sporadic exogenic events.

DATA AVAILABILITY

All data used in this work are publicly available via the Small Bodies Node of the Planetary Data system (<https://sbn.psi.edu/pds/archive/cassini.html>).

REFERENCES

- Altobelli N. et al., 2016, *Science*, 352, 312
- Auer S., 1975, *Rev. Sci. Instrum.*, 46, 385
- Baggaley W. J., 2000, *J. Geophys. Res.*, 105, 10353
- Banaszkiewicz M., Krivov A. V., 1997, *Icarus*, 129, 289
- Bernardoni E. et al., 2022, *Planet. Sci. J.*, 3, 69
- Boehnhardt H., 2004, *Split Comets*, University of Arizona Press, Tucson, p. 301
- Burns J. A., Lamy P. L., Soter S., 1979, *Icarus*, 40, 1
- Chandler C. O., Kueny J. K., Trujillo C. A., Trilling D. E., Oldroyd W. J., 2020, *ApJ*, 892, L38
- Cook A. F., Franklin F. A., 1970, *AJ*, 75, 195
- Coustonis A. et al., 1998, *A&A*, 336, L85
- Cuzzi J. N., Durisen R. H., 1990, *Icarus*, 84, 467
- Cuzzi J. N., Estrada P. R., 1998, *Icarus*, 132, 1
- Czechowski A., Mann I., 2003, *J. Geophys. Res. (Space Phys.)*, 108, L13+
- di Sisto R. P., Fernández J. A., Brunini A., 2009, *Icarus*, 203, 140
- Doner A. et al., 2024, *ApJ*, 961, L38
- Durisen R. H., 1984, *Adv. Space Res.*, 4, 13
- Durisen R. H., Estrada P. R., 2023, *Icarus*, 400, 115221
- Durisen R. H., Bode P. W., Cuzzi J. N., Cederbloom S. E., Murphy B. W., 1992, *Icarus*, 100, 364
- Elliott J. P., Esposito L. W., 2011, *Icarus*, 212, 268
- Epifani E. M., Dall'Ora M., Perna D., Palumbo P., Colangeli L., 2011, *MNRAS*, 415, 3097
- Estrada P. R., Durisen R. H., 2023, *Icarus*, 400, 115296
- Fiege K., Tieloff M., Hillier J. K., Guglielmino M., Postberg F., Srama R., Kempf S., Blum J., 2014, *Icarus*, 241, 336
- Filacchione G. et al., 2013, *ApJ*, 766, 76
- Fouchet T., Bézard B., Encrenaz T., 2005, *Space Sci. Rev.*, 119, 123
- Fulle M. et al., 2019, *MNRAS*, 482, 3326
- Graps A. L., Grün E., Svedhem H., Krüger H., Horányi M., Heck A., Lammers S., 2000, *Nature*, 405, 48
- Grigorieva A., Thébaud P., Artymowicz P., Brandeker A., 2007, *A&A*, 475, 755
- Grün E., Zook H. A., Fechtig H., Giese R. H., 1985, *Icarus*, 62, 244
- Grün E., Baguhl M., Hamilton D. P., Kissel J., Linkert D., Linkert G., Riemann R., 1995, *Planet. Space Sci.*, 43, 941
- Gurnett D. A., Anshel J. A., Kurth W. S., Granroth L. J., 1997, *Geophys. Res. Lett.*, 24, 3125
- Hedman M. M., Burns J. A., Tiscareno M. S., Porco C. C., 2009, *Icarus*, 202, 260
- Hedman M. M., Burns J. A., Evans M. W., Tiscareno M. S., Porco C. C., 2011, *Science*, 332, 708
- Hedman M. M., Burns J. A., Hamilton D. P., Showalter M. R., 2012, *Icarus*, 217, 322
- Hedman M. M., Burns J. A., Showalter M. R., 2015, *Icarus*, 248, 137
- Higuchi A., Kokubo E., 2020, *MNRAS*, 492, 268
- Horányi M., Burns J. A., Hamilton D. P., 1992, *Icarus*, 97, 248
- Horányi M., Morfill G., Gruen E., 1993, *J. Geophys. Res.*, 98, 21245
- Horányi M., Juhász A., Morfill G. E., 2008, *Geophys. Res. Lett.*, 35, 4203
- Hsu H.-W., Postberg F., Kempf S., Tieloff M., Burton M., Roy M., Moragas-Klostermeyer G., Srama R., 2011, *J. Geophys. Res. (Space Phys.)*, 116, 9215
- Hsu H.-W. et al., 2018, *Science*, 362, aat3185
- Humes D. H., 1980, *J. Geophys. Res.*, 85, 5841
- Jewitt D., 2009a, *ApJ*, 137, 4296
- Jewitt D., 2009b, *AJ*, 137, 4296
- Jones G. H. et al., 2008, *Science*, 319, 1380
- Kempf S. et al., 2004, *Icarus*, 171, 317
- Kempf S., Srama R., Horányi M., Burton M., Helfert S., Moragas-Klostermeyer G., Roy M., Grün E., 2005, *Nature*, 433, 289
- Kempf S. et al., 2008, *Icarus*, 193, 420
- Kempf S., Altobelli N., Schmidt J., Cuzzi J. N., Estrada P. R., Srama R., 2023, *Sci. Adv.*, 9
- Kimura H., Mann I., Jessberger E. K., 2003, *ApJ*, 583, 314
- Krivov A. V., Banaszkiewicz M., 2001, *Planet. Space Sci.*, 49, 1265
- Krivov A. V., Wardinski I., Spahn F., Krüger H., Grün E., 2002, *Icarus*, 157, 436
- Krüger H., Landgraf M., Altobelli N., Grün E., 2007, *Space Sci. Rev.*, 130, 401
- Krüger H., Strub P., Sommer M., Altobelli N., Kimura H., Lohse A.-K., Grün E., Srama R., 2020, *A&A*, 643, A96
- Landgraf M., Liou J.-C., Zook H. A., Grün E., 2002, *AJ*, 123, 2857
- Landgraf M., Krüger H., Altobelli N., Grün E., 2003, *J. Geophys. Res.*, 108, 5
- Levasseur-Regourd A.-C. et al., 2018, *Space Sci. Rev.*, 214, 64
- Linti S. et al., 2024a, *MNRAS*, 529, 1207
- Linti S., Khawaja N., Hillier J. K., Nölle L., Fischer C., Hsu H.-W., Srama R., Postberg F., 2024b, *MNRAS*, 529, 3121
- Liou J.-C., Zook H. A., Dermott S. F., 1996, *Icarus*, 124, 429
- Love S. G., Joswiak D. J., Brownlee D. E., 1994, *Icarus*, 111, 227
- Lowry S., Fitzsimmons A., Lamy P., Weissman P., 2008, *Solar System Beyond Neptune*, UAPress, Arizona, p. 397
- Mann I., 2010, *ARA&A*, 48, 173
- Mann I., Kimura H., 2000, *J. Geophys. Res.*, 105, 10317
- Mathis J. S., Rumpl W., Nordsieck K. H., 1977, *ApJ*, 217, 425
- Moro-Martín A., Malhotra R., 2002, *ApJ*, 124, 2305
- Moses J. I., Poppe A. R., 2017, *Icarus*, 297, 33
- Moses J. I., Lellouch E., Bézard B., Gladstone G. R., Feuchtgruber H., Allen M., 2000, *Icarus*, 145, 166
- Mukai T., Yamamoto T., 1979, *PASJ*, 31, 585
- Nesvorný D., Jenniskens P., Levison H. F., Bottke W. F., Vokrouhlický D., Gounelle M., 2010, *ApJ*, 713, 816
- Nesvorný D., Vokrouhlický D., Pokorný P., Janches D., 2011, *ApJ*, 743, 37
- Piquette M. et al., 2019, *Icarus*, 2019, 321, 116
- Pokorný P., Vokrouhlický D., Nesvorný D., Campbell-Brown M., Brown P., 2014, *ApJ*, 789, 25
- Poppe A. R., 2016, *Icarus*, 264, 369
- Poppe A. R., 2019, *MNRAS*, 490, 2421
- Poppe A. R., Horányi M., 2012, *Geophys. Res. Lett.*, 39, 15104
- Poppe A., James D., Jacobsmeyer B., Horányi M., 2010, *Geophys. Res. Lett.*, 37, L11101
- Poppe A. R. et al., 2019, *ApJ*, 881, L12
- Porco C. C. et al., 2006, *Science*, 311, 1393
- Postberg F., Kempf S., Hillier J. K., Srama R., Green S. F., McBride N., Grün E., 2008, *Icarus*, 193, 438
- Showalter M. R., Cuzzi J. N., Larson S. M., 1991, *Icarus*, 94, 451
- Showalter M. R., Hedman M. M., Burns J. A., 2011, *Science*, 332, 711
- Spahn F. et al., 2006a, *Planet. Space Sci.*, 54, 1024
- Spahn F. et al., 2006b, *Science*, 311, 1416
- Srama R. et al., 2004, *Space Sci. Rev.*, 114, 465
- Srama R. et al., 2011, *CEAS Space J.*, 2, 1
- Sterken V. J., Altobelli N., Kempf S., Schwehm G., Srama R., Grün E., 2012, *A&A*, 538, A102
- Stern S. A., 1996, *AJ*, 112, 1203

- Sykes M. V., Lebofsky L. A., Hunten D. M., Low F., 1986, *Science*, 232, 1115
- Szalay J. R., Horányi M., 2015, *Geophys. Res. Lett.*, 42, 10
- Szalay J. R., Horányi M., 2016, *ApJ*, 830, L29
- Szalay J. R., Piquette M., Horányi M., 2013, *Earth Planets Space*, 65, 1145
- Taylor A. D., Baggaley W. J., Steel D. I., 1996, *Nature*, 380, 323
- Teodoro L. F. A., Kegerreis J. A., Estrada P. R., Čuk M., Eke V. R., Cuzzi J. N., Massey R. J., Sandnes T. D., 2023, *ApJ*, 955, 137
- Tiscareno M. S. et al., 2013, *Science*, 340, 460
- Verbiscer A. J., Skrutskie M. F., Hamilton D. P., 2009, *Nature*, 461, 1098
- Wang J.-H., Brasser R., 2014, *A&A*, 563, A122
- Weissman P. R., 1980, *A&A*, 85, 191
- Williams G. V., Sato H., Sarneczky K., Wainscoat R., Woodworth D., Meech K., 2017, *Cent. Bur. Electron. Telegrams*, 4450, 1
- Yamamoto S., Mukai T., 1998, *A&A*, 329, 785
- Zubrin R., 2020, *Int. J. Astrobiology*, 19, 43

This paper has been typeset from a \LaTeX file prepared by the author.